Journal of Energy Storage 47 (2022) 103551

Contents lists available at ScienceDirect

Journal of Energy Storage

journal homepage: www.elsevier.com/locate/est

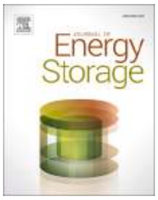

Research Papers

Hydrothermal synthesis of Co_3O_4 nanoparticles decorated three dimensional MoS_2 nanoflower for exceptionally stable supercapacitor electrode with improved capacitive performance

Md. Hasive Ahmad [a], Rabeya Binta Alam [a], Anwar Ul-hamid [b], S.F.U. Farhad [c], Muhammad Rakibul Islam [a,*]

[a] *Department of Physics, Bangladesh University of Engineering and Technology (BUET), Dhaka, Bangladesh*
[b] *Center for Engineering Research, Research Institute, King Fahd University of Petroleum & Minerals, Dhahran, Saudi Arabia*
[c] *Industrial Physics Division, Bangladesh Council of Scientific & Industrial Research (BCSIR), Dhaka, Bangladesh*

ARTICLE INFO

Keywords:
MoS_2
Co_3O_4
Nanoflower
Supercapacitor
Cyclic stability

ABSTRACT

In this study, a novel, Co_3O_4 nanoparticle decorated MoS_2 nanoflower (MoS_2/Co_3O_4) has been fabricated via a facile hydrothermal method by taking different concentrations of Co_3O_4 (0, 1, 2, 4, and 6%). The FE-SEM images represent a three-dimensional flower-like structure for MoS_2 and MoS_2/Co_3O_4. The different structural parameters of the nanoflowers were estimated from the XRD analysis. TEM analysis revealed that the inter-planar spacing of the nanostructure varied with the concentration of the Co_3O_4 nanoparticles. The Raman spectroscopy of MoS_2/Co_3O_4 nanoflower showed a distinct low-shift of the first-order Raman peaks suggesting n-type doping due to the incorporation of Co_3O_4. The specific capacitance as high as 220.72 $mFcm^{-2}$ at 0.14 $mAcm^{-2}$ together with high energy density and superior cycling stability (87% capacitance retention after 10,000 charge/discharge cycles) were obtained for the MoS_2/Co_3O_4 (4%) nanocomposite from the electrochemical analysis. This improved specific capacitance of MoS_2/Co_3O_4 can be attributed to the higher surface area, defect-rich structure, and lower charge transfer resistance of the prepared sample. The MoS_2/Co_3O_4 nanostructure with improved specific capacitance and higher stability synthesized from a simple, low-cost process will pave the way to the production of efficient and economic energy storage devices.

1. Introduction

With the rapid development of human civilization and the elevation of the world economy, the demand for energy conversion from renewable sources and their storage has become a great concern [1–3]. Among the available alternatives, supercapacitors, a new type of electrochemical capacitor have gained significant research attention as a promising energy storage device because of their high power density, fast charge/discharge efficiency, great cycling stability, and cost-efficiency compared to the conventional batteries [2–5]. The performance of supercapacitors relies greatly on the properties of electrode materials. Recently nanostructured transition metal dichalcogenides (TMD) has gained significant research attention as a potential source for supercapacitor electrodes because of their exceptional electronic and structural properties [6]. Among them, molybdenum disulfide (MoS_2) has considered as the most promising candidate as electrode materials due to its larger surface area, better hydrophilicity, higher electrical conductivity, higher intrinsic fast ionic conductivity, together with oxidation states in layered structure [7–15,16–19]. The two-dimensional layered structure of MoS_2 consists of a unit S-Mo-S atomic tri-layer where metal Mo and chalcogens S are strongly bound together by a covalent bond and layers of S-Mo-S are held together by weak van der Waals forces [20,21]. Which facilitates the easy intercalation of ions from the electrolyte into the interlayer of MoS_2 without distortion of crystal structures.

Nevertheless, the poor conductivity, inherent restacking property, unstable solid-electrolyte interface, and sponging reaction linked to electrolyte decomposition of the MoS_2 results in low capacitance and cyclic stability that may hinder its application as an electrode material [22–24].

One of the popular ways to improve the capacitive performance of the MoS_2 based composite electrode is to incorporate metal oxide

---

[*] Corresponding author.
E-mail address: rakibul@phy.buet.ac.bd (M.R. Islam).

https://doi.org/10.1016/j.est.2021.103551
Received 29 August 2021; Received in revised form 13 October 2021; Accepted 5 November 2021

nanoparticles in it. A variety of nanoparticles such as TiO_2, NiO, Co_3O_4, MnO_2, V_2O_5 have been introduced into the MoS_2 structure to improve its capacitance and stability [25–27]. Among them, cobalt oxide (Co_3O_4) nanoparticles, with ultra-high theoretical specific capacitance, high redox activity, and environmentally benign nature can be considered as one of the most promising alternatives as a secondary material for MoS_2 based supercapacitor [27–30].

Liang et al. [31] have fabricated a MoS_2—Co_3O_4 composite via anchoring Co_3O_4 particles onto the surface of MoS_2 nanosheets. Wang et al. [32] synthesize a Co_3O_4/C@MoS_2 core-shell structured material, where MoS_2 possess nanosheets like morphology, via a two-step calcination and solvothermal method by using ZIF-67 and $(NH_4)_2MoS_4$ as the precursors of Co_3O_4/C and MoS_2, respectively which show a significant increase in the capacitive performance compared with Co_3O_4 alone. Wang et al. [33] fabricated Co_3O_4 covered by a metallic MoS_2 nanosheet for lithium storage. Lou et al. [34] prepared Co_3O_4 decorated ultrathin MoS_2 nanosheet as an anode material for lithium-ion batteries. However, supercapacitors produced from MoS_2 nanosheets can restack during the charge/discharge process which results in poor electronic conductivity due to the high surface energy of 2D MoS_2 [35–39]. Additionally, the synthesis of MoS_2 nanosheets or core-shell structure is time-consuming and involves low-yield process. On that account, a stable nanostructure of MoS_2, for example, lamellar MoS_2 nanoflower prepared by a simple, low-cost, and high yield fabrication technique such as hydrothermal synthesis process may address those issues. Electrode prepared from flower-like nanostructured materials are more favorable to rally the energy storage capacity and extended the cycle life as it provides a large surface area and more channels to absorb the ions from the electrolyte [40]. Furthermore, the defect-rich surface of this electrode obtained from the decoration of nanoparticles may provide more active sites for the diffusion of ions from electrolytes [41].

In this work, we represent a facile method to prepare a novel Co_3O_4 nanoparticle decorated MoS_2 nanoflowers (MoS_2/Co_3O_4) via a simple hydrothermal route. The effect of the concentrations of Co_3O_4 nanoparticles on the different physical properties of the MoS_2/Co_3O_4 composite has been studied. The field mission scanning electron microscopy (FE-SEM) reveals that the MoS_2 and MoS_2/Co_3O_4 nanocomposites represent three-dimensional flower-like features consists of a number of nanostructured petals. The structural properties of the MoS_2/Co_3O_4 nanocomposites were investigated by transmission electron microscopy (TEM), X-ray diffraction (XRD) analysis, and Raman analysis. Benefiting from three-dimensional nanostructure, high surface area together with defect rich structure and synergistic effect the as-prepared MoS_2/Co_3O_4 provide improved electrochemical performance. Specific capacitance as high as 220.72 $mFcm^{-2}$ was obtained for the MoS_2/Co_3O_4 nanocomposite at a current density of 0.14 $mAcm^{-2}$ together with remarkable energy and power density. The MoS_2/Co_3O_4 provides excellent cycling stability, a 87% capacitance retention after 10,000 charge/discharge cycles at a current density of 2.83 $mAcm^{-2}$. The high performance of the MoS_2/Co_3O_4 electrode can be ascribed to the defect-rich structure, expanded interlayer, higher specific surface area, and improved electrical conductivity. We believe, this study may pave a prominent way to design and fabricate high-performance energy storage devices.

2. Experimental section

2.1. Materials

All the chemical reagents used in this study are of analytical grade and used as received without further purification. Sodium molybdate dehydrate ($Na_2MoO_4 \cdot 2H_2O$), and Dimethyl sulfoxide (C_2H_6OS) were obtained from Merck, Mumbai, India. Thiourea (CH_4N_2S), Urea (CH_4N_2O), polyvinyl alcohol $(C_2H_4O)_x$ and Sodium sulfate (Na_2SO_4) were obtained from Research Lab, India, and Cobalt nitrate hexahydrate ($Co(NO_3)_2 \cdot 6H_2O$) was obtained from SRL, India.

2.2. Synthesis of MoS_2 nanoflowers

A facile hydrothermal synthesis technique was employed to prepare the MoS_2 nanoflower. Sodium molybdate dihydrate ($Na_2MoO_4 \cdot 2H_2O$) and thiourea (CH_4N_2S) were used as the source for Mo and S, respectively. At first, sodium molybdate dihydrate and thiourea were dissolved in 120 ml distilled water followed by vigorous stirring yielding a clear solution, and was then poured into a 200 ml Teflon lined autoclave. The autoclave was then transferred to an oven at 200 °C for 24 h. The precipitate was centrifuged followed by washing with DI water and ethanol. The resultant black powder was dried for several hours at 60 °C to get MoS_2 nanoflower. Fig. 1 depcted the different steps involved in the synthesis of MoS_2 nanoflower by hydrothermal technique.

2.3. Preparation of Co_3O_4 nanoparticles

Hydrothermal synthesis technique was also used to prepare Co_3O_4 nanoparticles. An appropriate amount of Cobalt nitrate hexahydrate ($Co(NO_3)_2 \cdot 6H_2O$) and urea (CH_4N_2O) were dissolved in 140 ml DI water and followed by vigorous stirring until a homogenous and clear solution is formed. The solution was then poured into a Teflon-lined autoclave and transferred to an oven at 200 °C for 72 h. The precipitate was centrifuged, and washed by DI water and ethanol. The resultant black-pink solid powder was dried for several hours at 60 °C yielding the desired nanoparticles.

2.4. Preparation of MoS_2/Co_3O_4

To prepare 1 wt.% Co_3O_4 decorated MoS_2 nanocomposite appropriate amount of Co_3O_4 nanoparticle was transferred to 50 ml distilled water followed by 2 h of sonication using probe sonicator. 70 ml solution of Sodium molybdate dihydrate ($Na_2MoO_4 \cdot 2H_2O$) and thiourea (CH_4N_2S) were vigorously stirred and sonicated in 50 ml of Co_3O_4 solution followed by vigorous stirring for several hours. The solution was then poured into a Teflon-lined autoclave and heated at 200 °C for 24 h in an oven. The as-obtained black precipitate was washed several times by DI water and ethanol. The resultant materials were then dried at 80 °C for several hours to get desired materials. In this study, different concentrations of Co_3O_4 nanoparticles such as 1, 2, 4, and 6 wt.% was used and the resulting composite materials are termed as MoS_2/Co_3O_4 (1%), MoS_2/Co_3O_4 (2%), MoS_2/Co_3O_4 (4%), and MoS_2/Co_3O_4 (6%), respectively.

2.5. Electrode preparation

The working electrodes were prepared by depositing the slurry of active material mixed with PVA as binder and Dimethyl sulfoxide (C_2H_6OS) as solvent. To prepare the slurry the active materials were mixed with Polyvinyl alcohol (PVA) (5% of active material) and Dimethyl sulfoxide. PVA contains numerous hydroxyl groups that can form strong hydrogen bonds with both active materials and the current collector and are considered a very good choice as a binder for high-capacity anodes. Furthermore, PVA is water-soluble and the hydrophilic PVA may increase the wettability and increase the capacitance of the electrode [42,43]. All of these mixtures were sonicated for 1 h and then deposited on a glassy carbon electrode. Afterward, the working electrodes were dried for several hours at 70 °C.

2.6. Characterizations

The surface morphology of the samples was studied by field emission scanning electron microscopy (FE-SEM) (JSM 7600, Jeol). The micromorphology of MoS_2/Co_3O_4 composites was also characterized by high-resolution transmission electron microscopy (HR-TEM) using a JEOL, JEM 2100 F transmission electron microscope. For the TEM sample preparation, a small amount of materials was dispersed in 2 mL ethanol

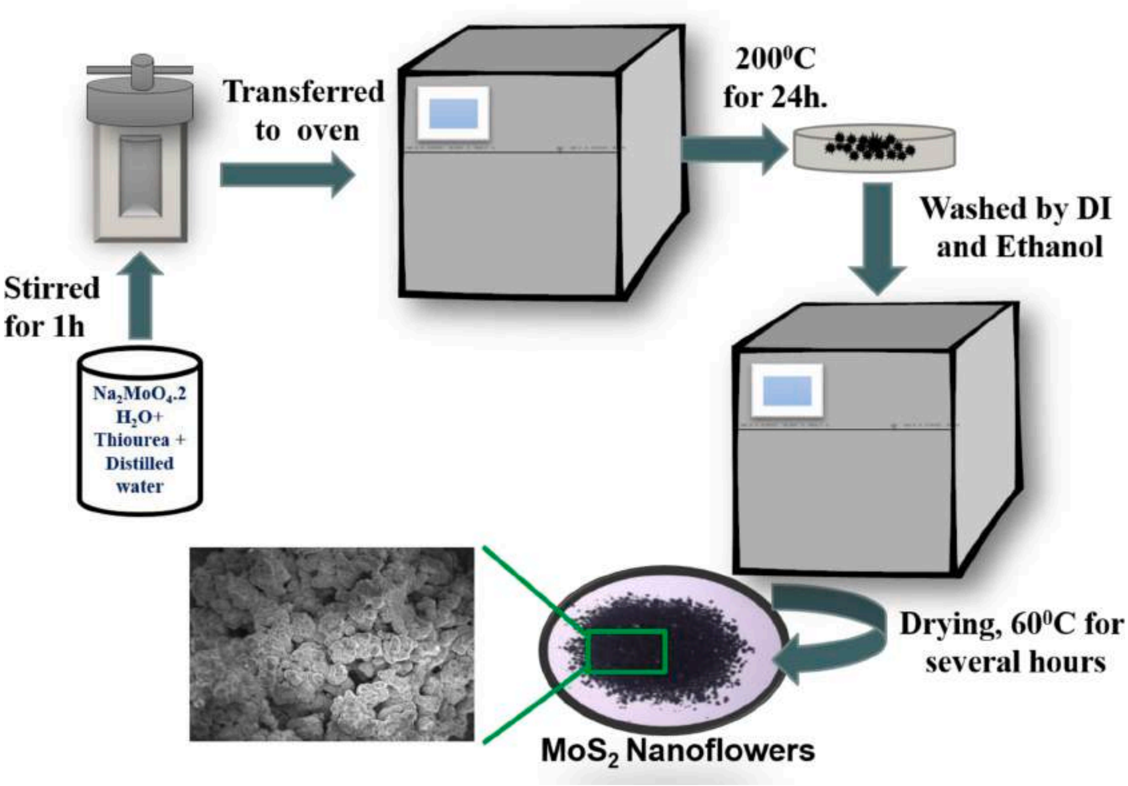

Fig. 1. Schematic diagram depicting the different steps involved in the preparation of MoS_2 nanoflowers.

and sonicated for 20 min. Then a drop of the sonicated sample was put on a 3 mm Cu grid with carbon coating. The sample was allowed to dry before inserting it into the microscope. The structural parameters of the MoS_2 nanoflower and MoS_2/Co_3O_4 composites were studied using the X-ray diffraction (XRD) technique. XRD data was taken using an X-ray diffractometer (3040XPert PRO, Philips) using CuK_α radiation (λ = 1.5406 Å). Raman analysis was performed at room temperature using a 785 nm diode laser (Power $\leq$ 5 mW) as an excitation source (HORIVA MacroRam) to study the vibrational structure of the synthesized nanoflowers.

The electrochemical performance of the MoS_2 and MoS_2/Co_3O_4 composites were studied by Cyclic Voltammetry (CV), Galvanostatic Charge Discharge (GCD), and Electrochemical Impedance Spectroscopy (EIS) using a CS310 electrochemical workstation (corrtest, china). The electrochemical measurements were performed in a conventional three-electrode cell setup: glassy carbon electrode, platinum plate (1 cm × 1 cm) as the counter electrode, Ag/AgCl reference electrode was used as the reference electrode, and 0.5 M Na_2SO_4 solution was used as the electrolyte.

3. Result and discussion

3.1. *Scanning electron microscopy*

To explore the morphological features of the as-prepared materials, FE-SEM was performed. Fig. 2(a) shows the FE-SEM images of pure MoS_2 having three-dimensional flower-like features with a number of nanosized petals in it and therefore described as nanoflower [44]. The FE-SEM images at higher magnification (Fig. 2b) shows that the thickness of the petals of the nanoflower are of several nm and are aligned together with a common inner center, forming a spherical flower shape with an average diameter of 2–5 μm [45–47]. Fig. 2(c) shows the FE-SEM images of Co_3O_4 nanoparticles. The Co_3O_4 nanostructured materials appear to be in a pyramidal shape with a diameter of 20–200 nm Fig. 1.

Fig. 3 shows the FE-SEM images of the MoS_2/Co_3O_4 composites with various concentrations of Co_3O_4. At low concentrations, the Co_3O_4 nanoparticles are found to be sprinkled both outside and inside of the MoS_2 nanoflowers. In Fig. 3a,b, the Co_3O_4 nanoparticles were found in the gap between the petals of MoS_2 nanoflower for a Co_3O_4

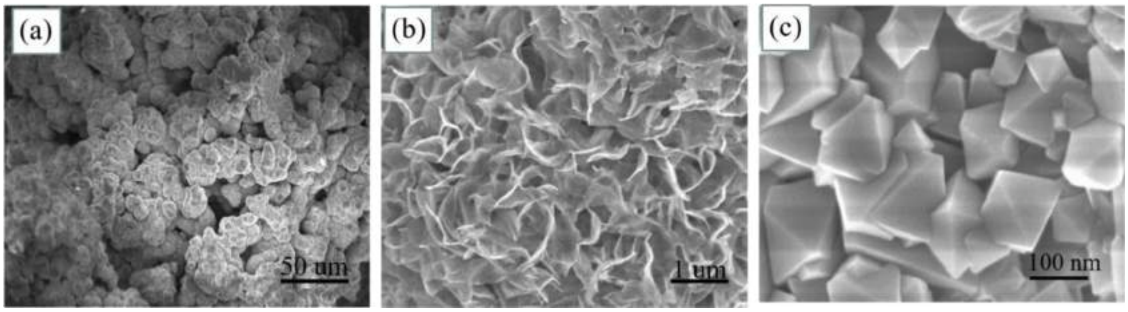

Fig. 2. FE-SEM images of MoS_2 nanoflowers at (a) the low magnification and (b) the high magnification. (c) FE-SEM image of Co_3O_4 nanoparticles.

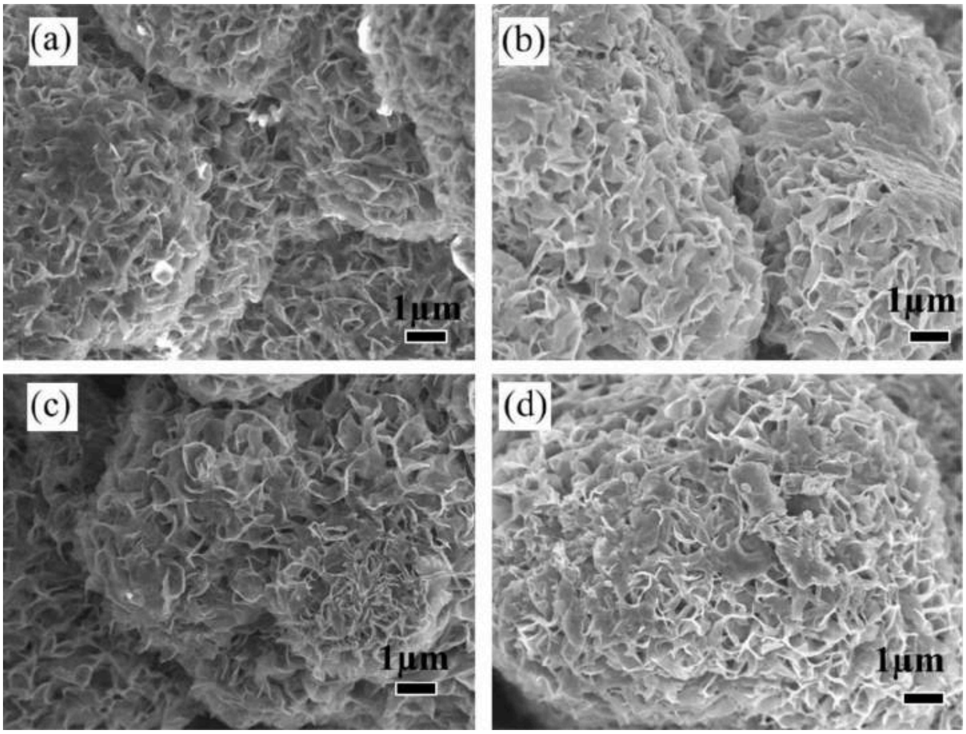

Fig. 3. FE-SEM images of (a) MoS_2/Co_3O_4 (1%) (b) MoS_2/Co_3O_4 (2%) (c) MoS_2/Co_3O_4 (4%) and (d) MoS_2/Co_3O_4 (6%) nanocomposites.

concentration of 1 and 2%. The size and morphology of the Co_3O_4 nanoparticles reduce and possess cube-like morphology in the MoS_2/Co_3O_4 (1%) composites. The smaller size of the dispersed Co_3O_4 nanoparticles in the composite may be attributed to the ultrasonication process and additional hydrothermal reaction that it goes through during composite preparation. With the increase of the concentration of Co_3O_4, aggregation between the MoS_2 layers is observed (Fig. 3c), maybe, due to the cross-link between MoS_2 layers by incorporated Co_3O_4 and the agglomeration nature of Co_3O_4 nanoparticles [48].

The elemental composition of the materials was identified using energy dispersive x-ray analysis (EDX). The EDX spectra for the MoS_2 and MoS_2/Co_3O_4 nanomaterials were demonstrated in supplementary Fig. SF1(a–e). The corresponding atomic percentages of the compositional elements in the nanomaterials are presented in supplementary Table ST1 showing the presence of Mo, S, and Co in the MoS_2/Co_3O_4 composite nanomaterials.

3.2. Transmission electron microscopy

Transmission electron microscopy (TEM) was used to study the

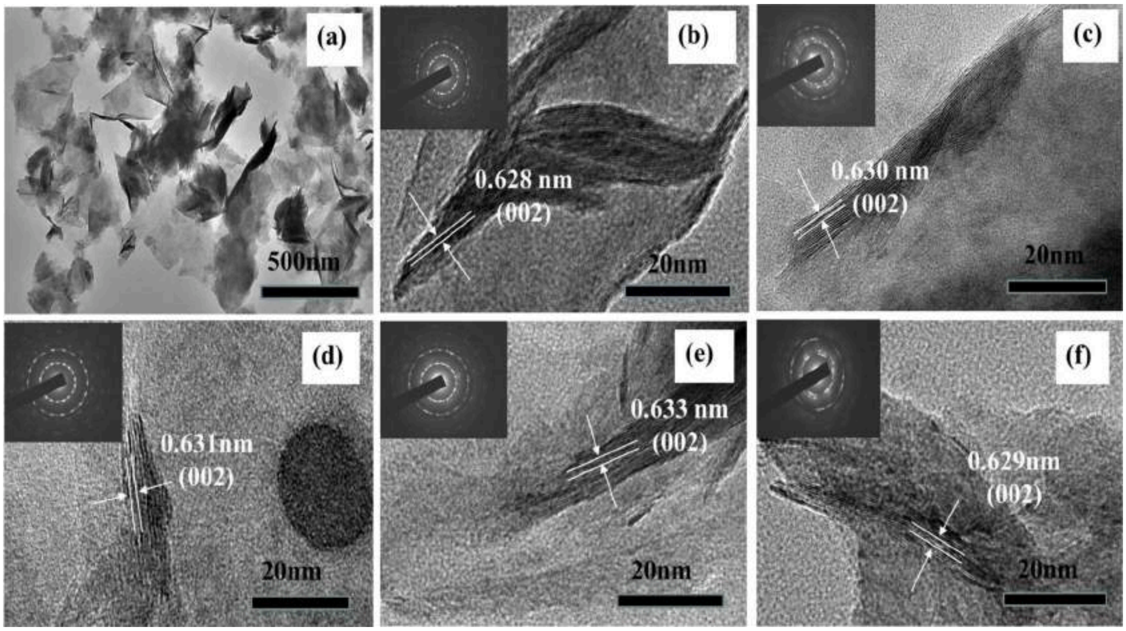

Fig. 4. (a) TEM image of MoS_2 nanoflower. HR-TEM images of (b) pure MoS_2, (c) MoS_2/Co_3O_4 (1%), (d) MoS_2/Co_3O_4 (2%), (e) MoS_2/Co_3O_4 (4%) and (f) MoS_2/Co_3O_4 (6%). Inset of (b–f) shows the corresponding SAED pattern.

micromorphology and analyze the structure of the MoS_2 nanoflower and MoS_2/Co_3O_4 composites. Fig. 4(a) shows the TEM image of pure MoS_2 nanoflower and is made up of an assembly of few-layer petals. The petals are found to be curled and overlapped because of nanosized thickness [49,50]. The lattice fringes of the MoS_2 and MoS_2/Co_3O_4 composites were observed using their corresponding HR-TEM images (Fig. 4(b–f)). Fig. 4(b) shows the lattice fringes for MoS_2 nanoflower having a lattice spacing of 0.628 nm and also indexed to the (002) planes corresponding to the hexagonal phase, which is large compared to the standard value of 0.615 nm (JCPDS card number 37–1492). This expansion in interplanar spacing can be attributed to the defect-rich structure of MoS_2 nanoflower. The crystalline boundaries can be evolved by defect for strain relief which leads to the expansion of lattice [51,52]. The widening of lattice fringes evident the existence of crystal defects [53]. Fig. 4(c–f) shows the HRTEM images of MoS_2/Co_3O_4 composites and the lattice spacing corresponds to the (002) planes of MoS_2 are found to 0.630 nm, 0.631 nm, 0.633 nm, and 0.629 nm for 1%, 2%, 4% and 6% of Co_3O_4, respectively. The incorporation of Co_3O_4 nanoparticles was found to increase the lattice spacing of the composite. The widening of the lattice spacing can be attributed to the production of defects in the MoS_2 crystal structure due to the incorporation of Co_3O_4. These defects can evolve the crystal boundaries due to strain relief resulting in lattice expansion. When introduced between the interplanar spacing of the nanoflowers Co_3O_4 nanoparticles create defects on the lattice of MoS_2 and thereby increase the interplanar spacing [54]. The inset of Fig. 4(b–f) represents the selected area electron diffraction (SAED) pattern of pure MoS_2 and the composites. The SAED patterns represent several diffuse rings for the MoS_2/Co_3O_4 suggesting the polycrystalline nature of the composites [49].

3.3. X-ray diffraction

The crystalline structure of MoS_2 and MoS_2/Co_3O_4 composites were studied by XRD. Fig. 5 shows the XRD patterns for MoS_2 nanoflower and MoS_2/Co_3O_4 composites. The observed XRD peaks for pristine MoS_2 nanoflower match with the JCPDS card number 37–1492 and the diffraction peaks are located at 2θ values of 13.99, 33.14, 39.46, 40.8 and 58.77 correspond to the (002), (100), (103), (105) and (110) reflections of the hexagonal structure of semi-conductive 2H-MoS_2 ($a = b = 0.316$ nm, $c = 1.229$ nm), respectively [55–57]. The (002) plane corresponds to the periodicity in the c-axis of MoS_2, suggesting the well-stacked layered structure and good crystallinity of MoS_2 [55,58,59]. Additionally, a shift in the (002) plane towards a smaller value of 2θ was found for MoS_2 nanoflower as compared to that of the bulk MoS_2 suggesting an expansion along the c-axis [60–61]. The presence of structural defects in the crystals may hinder the stacking of the MoS_2 layers and increase the inter-planer distance. No additional peaks correspond to the diffraction peaks of Co_3O_4 were observed in the XRD pattern of MoS_2/Co_3O_4 composites, this is maybe due to the low content of Co_3O_4 [62]. Furthermore, a reduction in the intensity of the diffraction peaks is observed due to the addition of Co_3O_4. Such a reduction in the intensity of the diffraction plane indicates deterioration of the crystallinity of MoS_2 due to lattice distortion, defective structures, and distinct pressure stress provided by the Co_3O_4 nanoparticles [60,63].

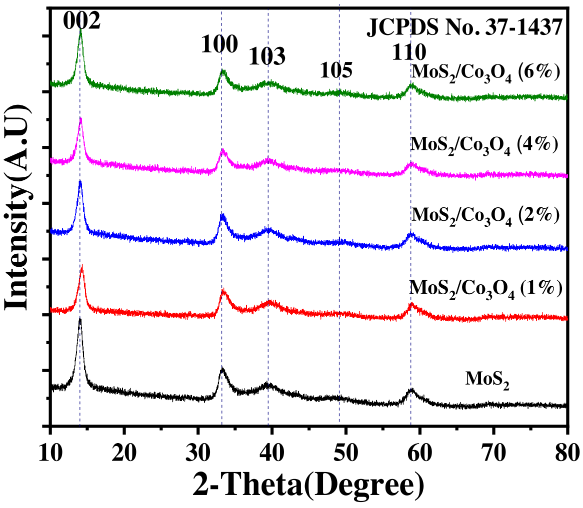

Fig. 5. XRD pattern of Pristine MoS_2 and as prepared MoS_2/Co_3O_4 composites.

With the incorporation of Co_3O_4 nanoparticles, the diffraction peaks slightly shift towards the higher 2θ values. This suggests that a reduction in the volume of the lattice cell occurred due to the addition of Co_3O_4. The lessening in the cell volume can be attributed to the larger ionic radius of Co^{3+} and Co^{2+} ion as compared to that of Mo^{4+} ion of MoS_2 [61].

The crystallite size (L) of the sample was measured from the (002) peak by using the Scherrer formula [64],

$$L = \frac{0.94\lambda}{\beta cos\theta}$$

where, λ is the wavelength of the x-ray used, θ is the diffraction angle and β is the full width at half-maximum of the diffraction peak.

Dislocation density (δ) and microstrain (ε) of the MoS_2/Co_3O_4 composites were calculated using the equations [65],

$$\delta = \frac{1}{L^2}$$

$$\varepsilon = \frac{\beta}{4\tan\theta}$$

The structural parameters of the as-prepared MoS_2 and MoS_2/Co_3O_4 nanocomposites are demonstrated in Table 1. Fig. 6 shows the variation of the structural parameter with the concentration Co_3O_4 in MoS_2. From Table 1, the estimated crystallite size of all the samples was found to be varied between 4.75 and 5.81 nm. The shrinkage of crystallite size at low concentration of Co_3O_4 nanoparticle in MoS_2 lattice can be attributed to the agglomeration of MoS_2 nanoflower due to the cross-linking of MoS_2 layers by Co_3O_4 nanoparticles [66]. Further increment of the concentration of Co_3O_4 might hinder the growth of MoS_2 crystals along with the c- axis caused the increment of crystallite size [66,67]. Additionally, an augmentation in the full width at half maxima (β) of the (002) diffraction peak is also observed as the amount of Co_3O_4 increases suggesting a reduction in crystallite size due to the incorporation of the nanoparticles [68–70]. The microstrain and crystallite size broadened the diffraction line without affecting the peak position. Broadening of the diffraction line caused by microstrain due to the displacement of atoms with respect to the reference lattice ascribed as lattice defects. Generation of microstrain attribute to the crystal imperfection, vacancies, and dislocation. The variation of microstrain due to the incorporation of nanoparticles is demonstrated in Fig. 6. It was found that microstrain is increasing with the concentration of Co_3O_4 up to 4% and a further increase in the concentration diminishes the microstrain, resulting in the increment of crystallite size [71]. The dislocation density represents the amount of imperfection in the prepared samples. It can be seen that the dislocation density and microstrain of the nanocomposites tend to increase and are much larger than that of pure MoS_2, which indicates that the incorporation of Co_3O_4 in the MoS_2 nanoflower causes lattice distortion. This lattice distortion results in the expansion of interlayer distance which could facilitate the fast electron transportation from the surface to the electrode [61].

Lattice constant has been calculated using the equation [72]:

$$\frac{1}{d^2} = \frac{4}{3}\,\frac{h^2 + k^2 + hk}{a^2} + \frac{l^2}{c^2}$$

where d is the atomic plane spacing, (h, k, l) represents the miller indices, and (a, b, c) are lattice constants. Estimated values of the lattice

Table 1
Diffraction parameters of pure MoS_2 and MoS_2/Co_3O_4 composites obtained from XRD analysis.

Samples	$\beta \times 10^2$ (radian)	L (nm)	$a = b$ (Å)	C (Å)	Lattice Strain (%)	Micro Strain $\varepsilon \times 10^{-3}$	Dislocation Density $\delta \times 10^{-3}$ (nm^{-2})
Pure MoS_2	2.51	5.81	3.094	12.66	2.15	51.20	29.63
MoS_2/Co_3O_4 (1%)	2.58	5.65	3.097	12.44	1.96	51.73	31.28
MoS_2/Co_3O_4 (2%)	2.67	5.47	3.094	12.63	2.00	54.29	33.44
MoS_2/Co_3O_4 (4%)	3.07	4.75	3.091	12.60	1.62	62.32	44.25
MoS_2/Co_3O_4 (6%)	2.56	5.69	3.088	12.59	1.96	52.05	30.87

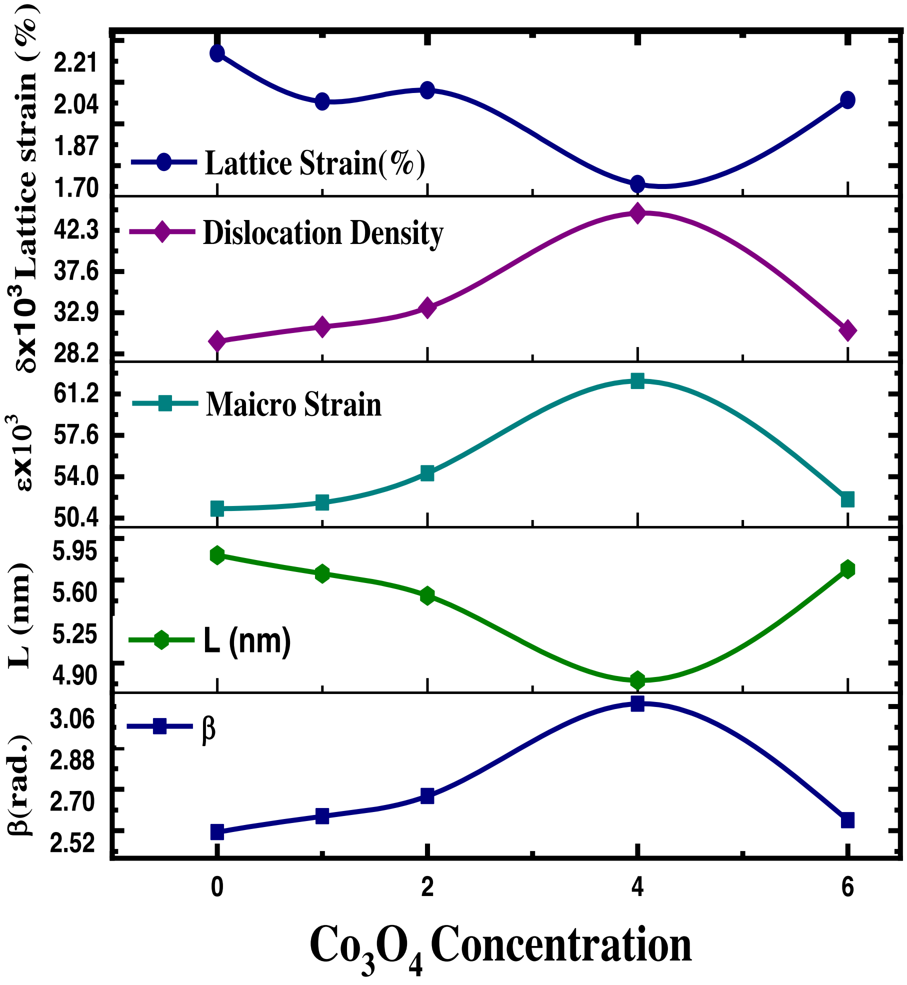

Fig. 6. Variation of XRD parameters as a function of Co_3O_4 Concentration.

constant are represented in Table 1 and are in good agreement with standard data [73]. The lattice constant *a* show a smaller reduction from standard data resulting in a smaller cell volume. The deteriorated crystallite size, lattice distortion, crystal defects, and dislocation density thus produced together with the variation in the D-spacing may improve the surface area, new active sites, and intercalation/deintercalation kinetics of the charge carriers during the charging/discharging process [74–76].

3.4. Raman spectroscopy

Raman spectroscopy was used to investigate the phase and composition of the MoS_2 and MoS_2/Co_3O_4 nanocomposites. Fig. 7 shows Raman spectra of MoS_2 nanoflower and prepared nanomaterials where two main characteristic peaks of pristine MoS_2 correspond to the $E^1{}_{2g}$ (~374.149 cm^{-1}) and A_{1g} (~402.934 cm^{-1}) occur from the vibrational modes of MoS_2. The two S atoms vibrate in-plane and in opposite directions compared to the Mo atom and originate the $E^1{}_{2g}$ phonon mode [77]. Whereas the A_{1g} phonon mode is introduced due to the out-of-plane vibration of the S atoms in opposite directions along the c-axis [78]. Additionally, no extra peaks were observed in the Raman spectrum of MoS_2/Co_3O_4 composites suggesting that incorporation of Co_3O_4 does not create any chemical bonds at the contact interface. It has been reported that the relatively broader as well as the weaker intensity of $E^1{}_{2g}$ peak suggest that the crystal structure of MoS_2 may contain substantial defects sites [79–80]. With the increase of the concentration of Co_3O_4, the $E^1{}_{2g}$ and A_{1g} peaks became weaker and broader which indicates that the increment of the defects and reduction of crystallinity which agreed better with the XRD analysis. Besides the frequency of the A_{1g} mode found to increase with the concentration of Co_3O_4 [81,82].

It was found that the Co_3O_4 nanoparticles affect the vibration of the S-Mo-S bond and the effect is more pronounced for the A_{1g} peak (out-of-plane vibration). Recent studies showed that a softening of the A_{1g} phonon mode occurs due to the n-type doping which results in a downshift of the intensity and peak frequency difference between the A_{1g} and $E^1{}_{2g}$ modes, on the other hand, p-type doping causes an upshift

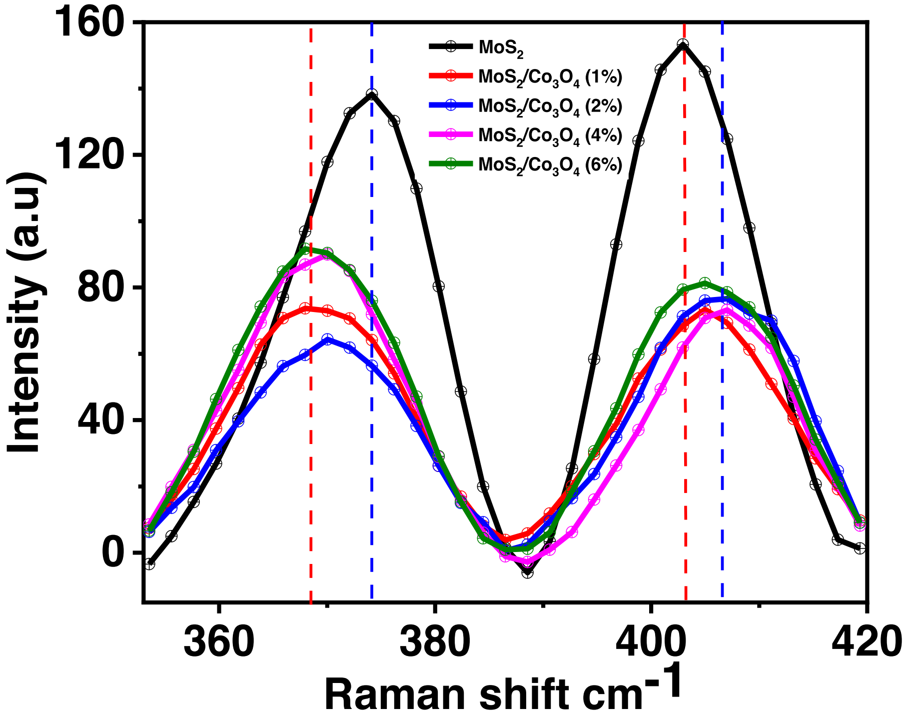

Fig. 7. Raman Spectra of pristine MoS_2 and MoS_2/Co_3O_4 composites.

of the Raman-active modes in opposite direction [83]. After incorporation of Co_3O_4 nanoparticles, a distinct low shift has been observed for the as-prepared composites suggesting n-type doping of the nanocomposite which results from the strong electron-phonon coupling in the A_{1g} phonon mode [83]. Due to the symmetry of lattice (structural distortion of A_{1g} mode does not affect the MoS_2 symmetry) A_{1g} optics mode couples more strongly with electrons than the $E^1{}_{2g}$ optics mode as a result all the electronic states have a non-zero value for the perturbation of A_{1g} mode which gives a large electron-phonon coupling [83]. For the incorporation of 4% and 6% Co_3O_4, an upshift of the observed A_{1g} mode is suggesting a decrement of the doping rate with the increase of the concentration Co_3O_4. Furthermore, the ratio of the relative intensity of the two-active mode ($A_{1g}/E^1{}_{2g}$) decreases with the increase of the concentration of Co_3O_4. The $A_{1g}/E^1{}_{2g}$ peak intensity ratio is found to be decreased from 1.1092 (for pristine MoS_2) to 0.8260 (MoS_2/Co_3O_4 (6%)). Such a decrease in $A_{1g}/E^1{}_{2g}$ peak intensity ratio suggests a distinct n-type doping caused by Co_3O_4 decoration [83–85].

3.5. Electrochemical performance analysis

Materials can store charges via two possible mechanisms. The first one is based on the faradic charge transfer mechanism, namely, "Pseudocapacitive", during which the alkali metal cation from the electrolyte (here Na^+) will diffuse between the layers of MoS_2 and intercalate with it:

$$MoS_2 + Na^+ + e^- \rightarrow MoS - SNa$$

The second charge storage mechanism is due to a non-faradic process in which the charges accumulate on the electrode/electrolyte interface, forming an electrical double layer. In this mechanism, the charge is stored on the surface or near it:

$$MoS_2 + Na^+ + e^- \rightarrow MoS_2 - Na$$

3.5.1. Cyclic voltammetry

To investigate the charge storage mechanism of the MoS_2/Co_3O_4 nanocomposites cyclic voltammetry (CV) was performed at various scan rates in 0.5 M Na_2SO_4 solution within a potential window between −0.3 V and 0.6 V ranging from 5 mVs^{-1} to 100 mVs^{-1} and is represented in Fig. 8. Quasi-rectangular CV curves were obtained for all the different samples. Such a deviation from the ideal rectangular shape indicates that the charge storage is dominated by the pseudocapacitive mechanism [86]. Furthermore, it was also observed that the area enclosed by the CV curve increase with the increase of scan rate, the current shows an increasing tendency indicating fast ion transportation and good capacitance retention of the prepared samples. The deviation rectangular shape of the CV curve at higher scan rates may attribute to the short-time limited movement of the electrolyte ions at the electrode surface [41].

3.5.2. Galvanostatic charging-discharging

The supercapacitive properties of the material can also be measured using galvanostatic charging-discharging (GCD) profile. GCD curve provides better quantitative insight than that of CV curve of the materials. The GCD curve deviated from the typical symmetrical triangular shape indicates the pseudocapacitive contribution.

Fig. 9(a–e) shows the galvanostatic charging-discharging curves of pristine MoS_2 and as prepared composites at current densities of 0.14, 0.21, 0.28, 0.42, 0.70, 1.13 and 1.41 $mAcm^{-2}$ where it can be seen that the discharge times of as-prepared samples is decreasing with current density. It can also be seen that the discharge time is decreasing with higher current density due to the low penetration of ions into the inner region of pores due to the fast potential changes [87].

Fig. 10(a) shows the CV curves for all the different samples at a scan rate of 30 mV/s. This figure shows that the area under the CV curve is increasing with the concentration of Co_3O_4. The MoS_2/Co_3O_4 (4%) nanocomposite was found to have the larger integrated area under the CV curve suggesting that the capacitive performance of this composite is better than that of the other samples. Further increment of the Co_3O_4 content caused a decrement of the integrated area under the CV curve. Fig. 10(b) illustrate the GCD plots for MoS_2, and MoS_2/Co_3O_4 with various concentration of Co_3O_4 at a current density of 0.14 $mAcm^{-2}$. The GCD curves were found to be deviated from the symmetric triangular shape and is an indication of the pseudocapacitive charge storage mechanism. The pseudocapacitive behavior may originate from the

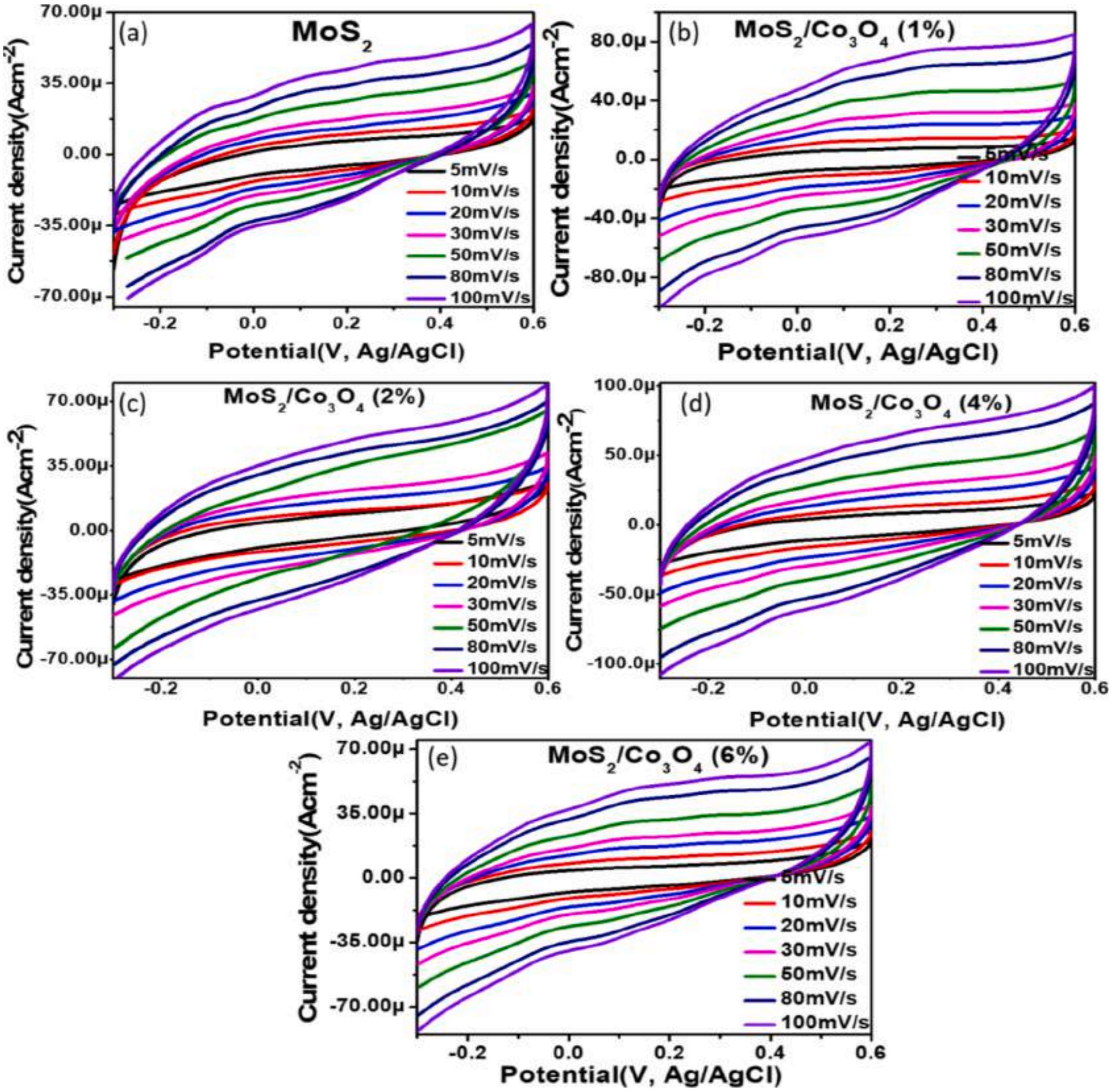

Fig. 8. Cyclic voltammetry curves of (a) MoS_2, (b) MoS_2/Co_3O_4 (1%), (c) MoS_2/Co_3O_4 (2%), (d) MoS_2/Co_3O_4 (4%) and (e) MoS_2/Co_3O_4 (6%) composites at different scan rates.

intercalation between MoS_2 and the Na^+ ions in the electrolyte. The empty orbitals of MoS_2 intercalate with the ions and the ions can diffuse between the MoS_2 layers [88]. From Fig. 10(b) it was also found that the discharge time increases with the amount of Co_3O_4 content and the highest discharging time was achieved for the MoS_2/Co_3O_4 (4%) nanocomposite.

The specific capacitance (C_s) of MoS_2 and MoS_2/Co_3O_4 nanocomposites were estimated from the GCD curves by using the formula [25]:

$$C_s = \frac{2I\Delta t}{s\Delta V}$$

where I is the discharge current, Δt is the discharging time, s is the area of the active material and ΔV is the potential window. The estimated value of the C_s for all the samples are tabulated in Table 2. From Table 2 it is evident that the MoS_2/Co_3O_4 (4%) nanocomposite yields the highest value of specific capacitance (220.72 $mFcm^{-2}$ at a current density of 0.14 $mAcm^{-2}$). The specific capacitance of the nanocomposite was found to be decreased with the increase of current density. Such a variation in specific capacitance is more common as at low current density electrolyte ions diffuse to all active sites of the electrode more efficiently which gives rise to the complete insertion/extraction reaction and results in a superior capacitance [88]. At higher current density the diffusion of ions occurs on the surface of the electrode and charge transportation is relatively low which leads to the lower capacitance [89]. The energy density (E) and power density (P) of MoS_2 and MoS_2/Co_3O_4 nanocomposites were calculated using the formula [25]:

$$E = \frac{C_s \Delta V^2}{2} \tag{6}$$

$$P = \frac{E}{2\Delta t} \tag{7}$$

where C_s is the specific capacitance, ΔV is the potential window, Δt is the discharging time. The energy density and power density for the MoS_2 and MoS_2/Co_3O_4 nanocomposite are presented in Table 2. It was found that the MoS_2/Co_3O_4 (4%) composite is delivering the highest value for both the energy density and power density.

Energy and power density of MoS_2 and MoS_2/Co_3O_4 (4%) have also been calculated using two-electrode setups. Supplementary Fig. SF2 (a) shows the CV curves for MoS_2 and MoS_2/Co_3O_4 (4%) composite at a scan rate of 20 mVs^{-1} in a potential range from 0 to 1.2 V. CV curves have been deviated from the typical rectangular CV curve due to the pseudocapacitive behavior. Fig. SF2 (b) shows the GCD curve of MoS_2 and MoS_2/Co_3O_4 (4%) at 0.15 $mAcm^{-2}$ obtained using the two-electrode set

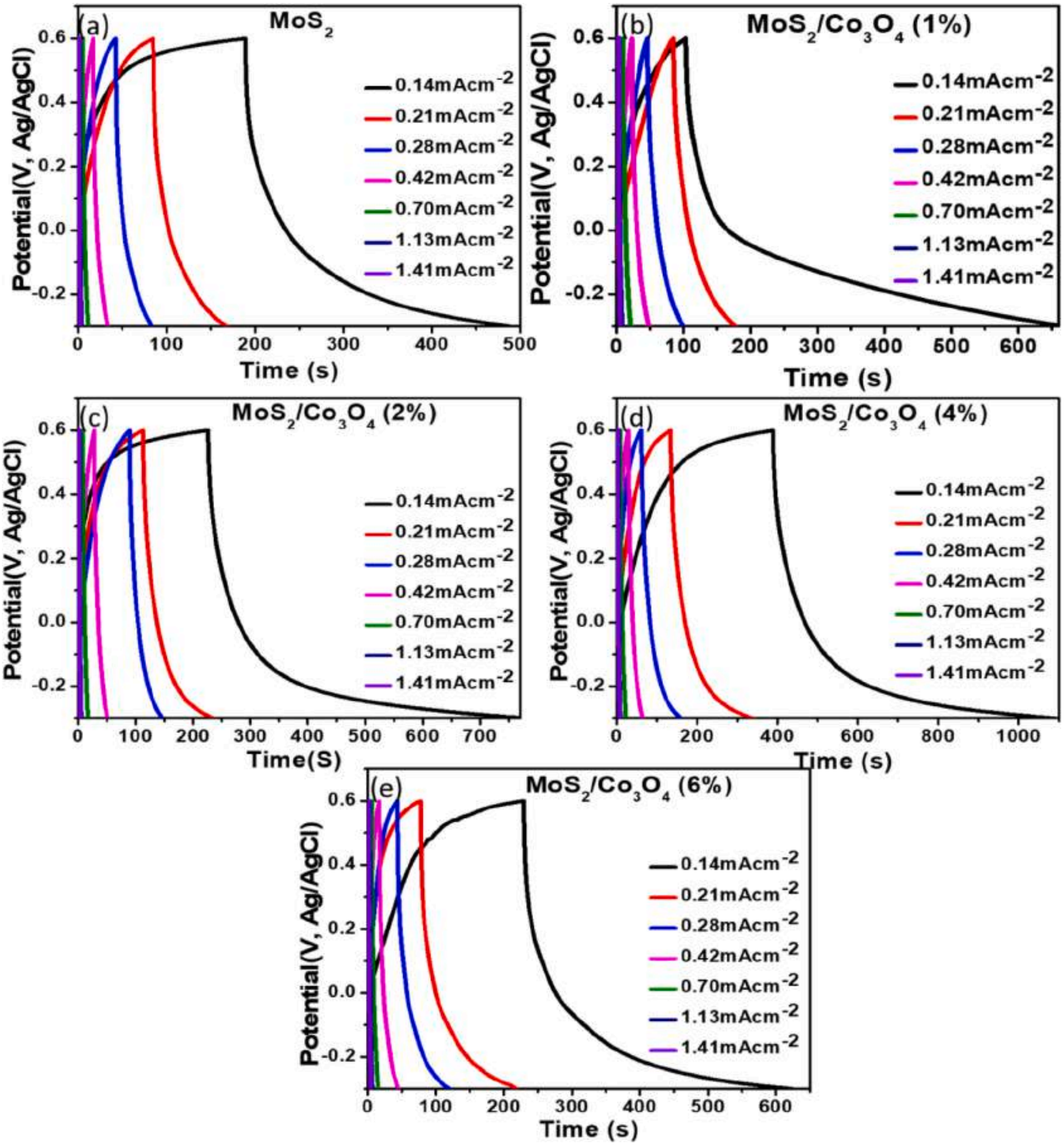

Fig. 9. Galvanostatic charging- discharging curves of (a) MoS_2, (b) MoS_2/Co_3O_4 (1%), (c) MoS_2/Co_3O_4 (2%), (d) MoS_2/Co_3O_4 (4%) and (e) MoS_2/Co_3O_4 (6%) composites at different current densities.

up. The as-obtained non-liner GCD curve further confirm the pseudocapacitive performance [86]. The specific capacitance of MoS_2 and MoS_2/Co_3O_4 (4%) have been calculated from this GCD curve and are found to be 33.25 $mFcm^{-2}$ for MoS_2 which increased to 47.50 $mFcm^{-2}$ for MoS_2/Co_3O_4 (4%) which deliver an energy density of 2.38 $mWhcm^{-2}$ and at a power density of 45 $mWcm^{-2}$. For pure MoS_2 an energy density of 1.66 $mWhcm^{-2}$ at power density of 45 $mWcm^{-2}$. These aforementioned result of MoS_2/Co_3O_4 (4%) further indicates that it can serve as one of the most promising electrode materials for supercapacitors.

3.5.3. Electrochemical impedance spectroscopy

Electrochemical impedance spectroscopy (EIS) analysis is a predominant method to elucidate the resistive behavior of the electrode that helps to investigate the charge-storage mechanism of the electrochemical system. Fig. 11 shows the Nyquist plot for MoS_2 and the MoS_2/Co_3O_4 nanocomposites and are depicted by plotting Z''(the imaginary impedance) as a function of Z' (the real impedance) in the frequency range of 0.1 Hz to 100 kHz. In general, three characteristics regions can be observed in the Nyquist plot: (1) an inclined line along the imaginary axis at the low-frequency region, represents the capacitive behavior which may interpret as the double-layer capacitive region. (2) A partial semi-circle in the high-frequency region represents the blocking behavior of the electrode and behaves as a pure resistor. (3) Middle-frequency range of the Nyquist plot represents the diffusion of ions in the electrode from the electrolyte and the effect of porosity and thickness of the electrode on the diffusion of the ions. An AC equivalent circuit (named as Randles circuit depicted in the inset of Fig. 11 [90]), modeled as the frequency-based electrical behavior of the device and was used to explain the faradic process of the device. The Nyquist plots show a semicircle in the high-frequency region together with an inclined line in the low-frequency region for all the samples. The intercept of the semicircle to the imaginary axis reveals the equivalent series resistance, R_s (also known as solution resistance), which represents the ohmic resistance of the electrolyte and the internal resistance of the electrode. The diameter of the semicircle corresponds to the impedance of the electrode/electrolyte interface (R_{el}) and the charge-transfer resistance

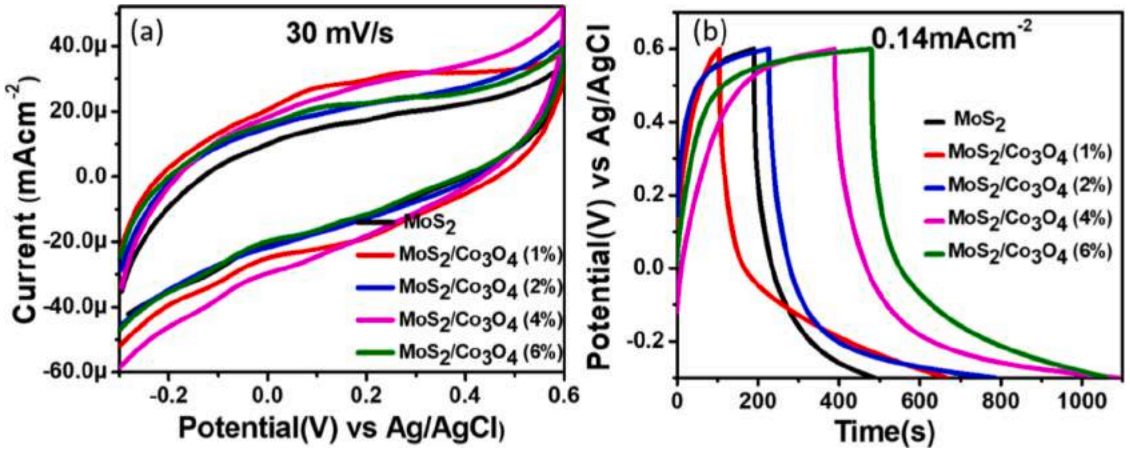

Fig. 10. (a) Cyclic voltammetry measurements at 30 mV/s, (b) Constant-current charge-discharge voltage profiles at 0.14 mAcm^{-2} for MoS$_2$ and as-prepared MoS$_2$/Co$_3$O$_4$ composites.

Table 2
Specific capacitance, Energy Density and Power Density of MoS$_2$ and MoS$_2$/Co$_3$O$_4$ composites at a current density of 0.14 mAcm^{-2}.

Sample	Areal Capacitance (mF/cm^2)	Energy Density (µWhcm^{-2})	Power Density (µWcm^{-2})
Pure MoS$_2$	93.62	10.53	127.30
MoS$_2$/Co$_3$O$_4$ (1%)	168.14	18.91	127.32
MoS$_2$/Co$_3$O$_4$ (2%)	177.66	19.99	127.16
MoS$_2$/Co$_3$O$_4$ (4%)	220.72	24.83	127.33
MoS$_2$/Co$_3$O$_4$ (6%)	124.14	13.96	127.32

(R_{ct}) that occurred during the faradic process, which, illustrates the rate of redox reactions of the electrode and electrolyte that emerge at the interface. The constant phase element (CPE), is a capacitive element used in the equivalent circuit for the better fitting of the curve. CPE is attributed to the nonideal capacitive behavior of the electrochemical system. The diffusion of the Na$^+$ions into the porous structure of the electrode represented by the Warburg element (W_o) results from the frequency dependence of the diffusion process. Warburg region in the Nyquist plot is represented by 45° region in the Nyquist plot. The semicircle of the high-frequency zone corresponds to the charge transfer resistance at the electrode and electrolyte interface and the linear portion of the low-frequency zone stands for pure capacitive manners [91–94]. Table 3 represents the values of different components of the equivalent circuit obtained from the best fit of the experimental data using ZView software. From Table 3 it is observed that all the samples had a similar series resistance Rs. However, the charge-transfer resistance reduces due to the concentration of Co$_3$O$_4$. In particular, the MoS$_2$/Co$_3$O$_4$ (4%) nanocomposite showed the smallest charge transfer resistance (R_{ct} = 2.18 KΩ) which is only 4.01% of pristine MoS$_2$ (R_{ct} = 8.73 KΩ) and smaller than that of any other composite materials. This result suggests that MoS$_2$/Co$_3$O$_4$ (4%) nanocomposite is the electrically more conductive among all the as-prepared electrodes and allows fast electron-conducting ability at the electrode surface [91]. As a result, the contact resistance and charge transfer resistance got reduced that favor the rapid Na$^+$ ions insertion/extraction and fast charge transfer at the electrode-electrolyte interface resulting in the significant increase of the capacitance value for the MoS$_2$/Co$_3$O$_4$ (4%) nanocomposite. Moreover, the low-frequency zone of the Nyquist plot suggests an ideal capacitance with a result of a higher rate of diffusion and mass transfer.

Table 3
EIS fitting parameters of pristine MoS$_2$ and MoS$_2$/Co$_3$O$_4$ composites.

Sample	R_s (Ω)	R_{el} (Ω)	R_{ct} (KΩ)
MoS$_2$	5.02	19.82	8.73
MoS$_2$/Co$_3$O$_4$ (1%)	5.49	11.47	4.16
MoS$_2$/Co$_3$O$_4$ (2%)	6.92	18.90	3.99
MoS$_2$/Co$_3$O$_4$ (4%)	6.08	15.89	2.18
MoS$_2$/Co$_3$O$_4$ (6%)	5.50	18.57	3.25

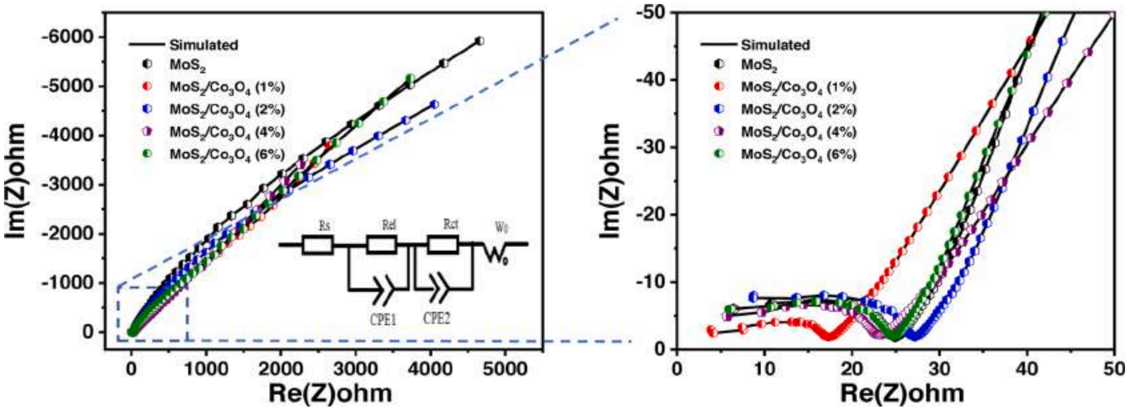

Fig. 11. Modeled Nyquist plots for MoS$_2$ and as prepared MoS$_2$/Co$_3$O$_4$ composites. Inset shows the equivalent circuit diagram of Randle's model.

3.5.4. Electrode stability analysis

The Nyquist plots of the MoS_2/Co_3O_4 (4%) nanocomposite (sample with best capacitive performance) were taken after 10,000 cycles of operation and compared with that of the 1st run and are presented in Fig. 12(a). The radius of the semi-circle of the impedance spectrum after 10,000 cycles of electrode material is found to be smaller than that of the 1st cycle. The obtained value of different components of the equivalent circuit is listed in Table 4, and the values of the *Rs, Rel*, and *Rct* obtained from the 10,000 cycles were found to be smaller than that of the 1st cycle. This result suggests that after 10,000 cycles of operation this electrode attain reduction of the internal resistance as well as become more electrically conductive and possess fast electron-conducting ability at the interface [91]. Such a reduction in internal resistance can be attributed to the electrochemical activation of active material, reduced agglomeration of active material during cycling, and batter interface [94,95]. Investigation of cyclic stability of the MoS_2/Co_3O_4 (4%) composite is presented in Fig. 12(b) which represents an 87% retention of the capacitance values after 10,000 charge/discharge cycle at a current density of 2.83 $mAcm^{-2}$. For the first few hundred cycles the retention decreased near to ~90% and then start to increase after the 1200 cycles and with consistency reached up to 96–98% after the first 1500 cycles and then started to decrease gradually and reached 87% of the initial capacity after 10,000 cycles. Initially, the coulombic efficiency was found to be 113% and reaches 104% after 10,000 cycles which suggests the superior stability of the MoS_2/Co_3O_4 (4%) composite. This excellent cycling stability and the coulombic efficiency of the MoS_2/Co_3O_4 (4%) nanocomposite may arise from the stable structure of the prepared electrode increased and because of the improvement of the diffusion of ions in the pores of the materials and possible increment of the wettability of the material over time [95].

3.5.5. Electrochemical behavior of MoS_2/Co_3O_4 (4%) as electrode

From the electrochemical analysis, it was found that the capacitance of the MoS_2 nanoflower increases with the increment of Co_3O_4 content suggesting that the Co_3O_4 nanoparticles play a significant role in the electrochemical performance. This suggests that the introduction of Co_3O_4 enhance the transfer of ions and electron of electrolyte to the interface of the electrode [34]. Furthermore, the MoS_2/Co_3O_4 (4%) electrode exhibits the best capacitive performance as it provides the highest value of specific capacitance together with large energy and power. Among the different samples, MoS_2/Co_3O_4 (4%) represents the lowest R_{ct} (2.18 KΩ) value compared to that of the pristine MoS_2 and other MoS_2/Co_3O_4 electrode suggesting better electrochemical activity, rapid electron transportation, and diffusion of ions in the electrode resulting in the supercilious electrochemical performance of MoS_2/Co_3O_4 (4%) [32,96,97]. This batter result from MoS_2/Co_3O_4 nanocomposite may arise from the synergistic effect of MoS_2 and Co_3O_4 together with the improved surface area, larger interplanar spacing, dislocation density and defect rich composite structure. The defect-rich structure results from the incorporation of Co_3O_4 nanoparticles between the interplanar spacing of MoS_2 nanoflowers creates an interlink connection between the lattice of MoS_2 which can improve the electrical conductivity and the expended interplanar spacing which may offer more open channels for the diffusion of ions and electron to the electrode interface. The lower concentration of Co_3O_4 (1% and 2%) limits the transfer of electrons and ions of electrolyte to the electrode surface. The increased concentration of Co_3O_4 facilitates the improved intercalation of ions and electrons and increased electronic conductivity but further increment of Co_3O_4 concentration (6%) hinders the diffusion of ions and electrons diminish the performance of the electrode [32,98,99]. The changes in the crystallite size of the MoS_2/Co_3O_4 due to the incorporation of Co_3O_4 may also help to improve the capacitance nanocomposite by reducing the crystallite size. The MoS_2/Co_3O_4 (4%) nanocomposites possess the smallest crystallite size that offers the largest surface area which provides more active surface sites for electrochemical reactions. Further increment of Co_3O_4 enhances the crystallite size gives lower surface area limits the reaction sites [58,100]. In addition, the changes in capacitance value may attribute to the higher dislocation density the higher current response of the samples [101]. The dislocation density of the prepared samples was found to be increased with the concentration of Co_3O_4 and MoS_2/Co_3O_4 (4%) nanocomposite shows the highest value of dislocation density which also results in the improvement of the capacitance value.

Table 4
EIS fitting parameters of MoS_2/Co_3O_4 (4%) composites obtained from the 1st and 10,000th cycle.

Cycle	R_s (Ω)	R_{el}(Ω)	R_{ct} (KΩ)
1	5.30	10.04	2.20
10,000	4.74	9.54	0.45

From the above discussion, it is evident that the MoS_2/Co_3O_4 (4%) offers the best performance in terms of capacitance and stability and can be a suitable choice for the supercapacitor electrode. Table 5 represent the specific capacitance of MoS_2 based electrode obtained from materials with different surface morphology [26,58,95,99,101–107]. From this table, it is clear that the specific capacitance of MoS_2/Co_3O_4 (4%) electrode obtained from this work is better compared to that of the reported values. This batter results may attribute to the increased surface area of the nanoflower-shaped nanocrystallite structure that provides

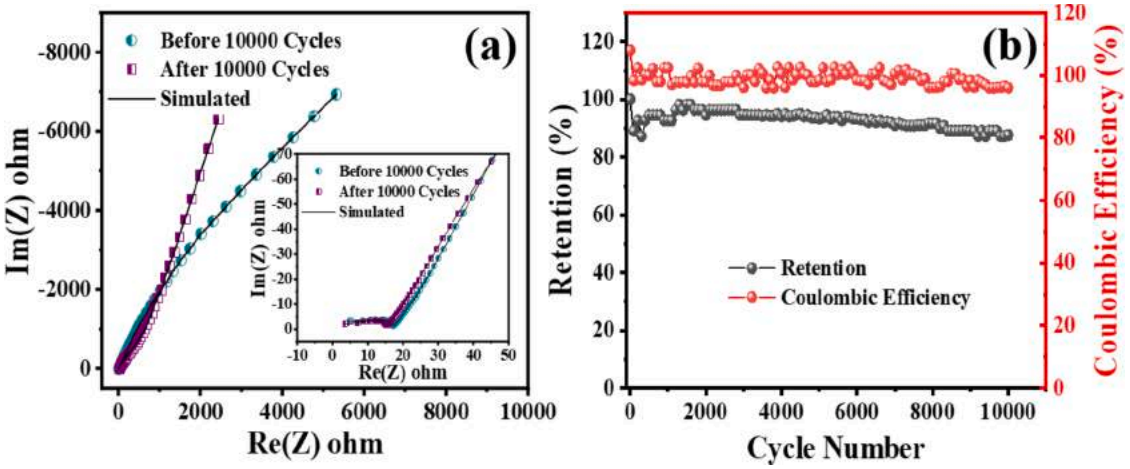

Fig. 12. (a) Modeled Nyquist plots for the MoS_2/Co_3O_4 (4%) sample before and after 10,000 cycle of operation. Inset image show the equivalent circuit diagram of Randle's model. (b) Capacitive retention and Columbic efficiency of the MoS_2/Co_3O_4 (4%) sample over 10,000cycle of operation.

Table 5
Comparison of capacitance of reported MoS_2 based supercapacitors in the literatures.

Electrode	Morphology	Area capacitance	Reference
MoS_2/Co_3O_4	Nanoflowers	220.72 $mFcm^{-2}$	This work
MoS_2@CNT/RGO	Nanoflowers	129 $mFcm^{-2}$ (0.1 $mAcm^{-2}$)	97
1H-MoS_2@Oleylamine	Nanosheet	50 $mFcm^{-2}$ (0.37 Ag^{-1})	101
PEDOT(BF^{4-})/MoS_2	Monolayer	149.8 $mFcm^{-2}$ (1.0 mA cm^{-2})	102
MoS_2/CoS_2 Nanotube Arrays on Ti plate	Nanosheet	142.5 $mFcm^{-2}$ (1 $mAcm^{-2}$)	103
MoS_2/graphene	Flake	11 $mFcm^{-2}$ (5 mV/s)	104
1T-MoS_2 nanofilm	Nanosheet	1.1 mF cm^{-2} (0.04 $mAcm^{-2}$)	93
MoS_2/rGO	Nanosheet	14.09 $mFcm^{-2}$ (5 mV/s)	56
PEDOT: PSS/MoS_2/PEDOT	Nanoparticles	51.01 $mFcm^{-2}$ (0.1 $mAcm^{-2}$)	100
NiO/MoS_2/rGO	Nanosheet	7.38 $mFcm^{-2}$ (25 mVs^{-1})	26
Co_3O_4/NiO	Nanowires	0.71 $mAhcm^{-2}$ (3 $mAcm^{-2}$)	107

more active sites as well as better conductivity and defect-rich structure. We believe that this outstanding result is a consequence of the synergistic effect of MoS_2 and Co_3O_4 nanoparticles, defect-rich structure, better electrical conductivity, and small crystallite size. Moreover, the nanoflower provides more surface area than the nanosheets or flakes.

4. Conclusion

In summary, we have designed a facile and efficient way to successfully synthesize Co_3O_4 nanoparticles anchored in 3D-MoS_2 nanoflower architectures by varying the concentration of Co_3O_4 between 0 and 6% via a facile hydrothermal method. The flowerlike three-dimensional structure of the as-prepared MoS_2 and MoS_2/Co_3O_4 was confirmed by FE-SEM images. XRD analysis provides different structural parameters of the prepared samples. Interlayer spacing of the prepared nanostructure was measured using TEM analysis. Incorporation of Co_3O_4 nanoparticle causes n-type doping which was confirmed via the distinct low-shift of first-order Raman peaks. In the three-electrode system, MoS_2/Co_3O_4 (4%) composite electrode exhibits the highest specific capacitance of 220.72 $mFcm^{-2}$ and energy density of 24.83 $\mu Whcm^{-2}$ at 0.14 $mAcm^{-2}$ together with excellent cyclic stability with a capacitive retention of 87% after 10,000 cycles of operation. The improved electrochemical performance obtained from the MoS_2/Co_3O_4 may arise from the synergistic effect of MoS_2 nanoflower and Co_3O_4 nanoparticles. Furthermore, the greater surface area, dislocation density, and defect-rich structure of the composite structure as well as improve the electrical conductivity and the expended interplanar spacing may offer more open channels for the diffusion of ions and electrons to the electrode interface.

CRediT authorship contribution statement

Md. Hasive Ahmad: Methodology, Formal analysis, Investigation, Writing – original draft. **Rabeya Binta Alam:** Formal analysis, Investigation. **Anwar Ul-hamid:** Investigation. **S.F.U. Farhad:** Investigation. **Muhammad Rakibul Islam:** Conceptualization, Methodology, Writing – review & editing, Supervision.

Declaration of Competing Interest

The authors declare that they have no known competing financial interests or personal relationships that could have appeared to influence the work reported in this paper.

Acknowledgments

The authors would like to acknowledge Dr. C. K. Roy (Department of Chemistry, BUET, Bangladesh) for help with two electrode measurements. M. H. Ahmad, R. B. Alam, and S. F. U. Farhad gratefully acknowledge the approval of BCSIR authority for the instrumental support under the project #100-FY2017-2020.

Supplementary materials

Supplementary material associated with this article can be found, in the online version, at doi:10.1016/j.est.2021.103551.

References

[1] A sustainable material world, Nat. Mater. 16 (7) (2017) 691, https://doi.org/10.1038/nmat4932.

[2] S. Chu, Y. Cui, N. Liu, The path towards sustainable energy, Nat. Mater. 16 (1) (2017) 16–22, https://doi.org/10.1038/nmat4834.

[3] A. González, E. Goikolea, J.A. Barrena, R. Mysyk, Review on supercapacitors: technologies and materials, Renew. Sustain. Energy Rev. 58 (2016) 1189–1206, https://doi.org/10.1016/j.rser.2015.12.249.

[4] R.R. Palem, et al., Enhanced supercapacitive behavior by CuO@MnO_2/carboxymethyl cellulose composites, Ceram. Int. 47 (19) (2021) 26738–26747, https://doi.org/10.1016/j.ceramint.2021.06.081.

[5] J. Yan, Q. Wang, T. Wei, Z. Fan, Recent advances in design and fabrication of electrochemical supercapacitors with high energy densities, Adv. Energy Mater. 4 (4) (2014), 1300816, https://doi.org/10.1002/aenm.201300816.

[6] X. Chia, A.Y.S. Eng, A. Ambrosi, S.M. Tan, M. Pumera, Electrochemistry of nanostructured layered transition-metal dichalcogenides, Chem. Rev. 115 (21) (2015) 11941–11966, https://doi.org/10.1021/acs.chemrev.5b00287.

[7] H.M. El Sharkawy, A.S. Dhmees, A.R. Tamman, S.M. El Sabagh, R. M. Aboushahba, N.K. Allam, N-doped carbon quantum dots boost the electrochemical supercapacitiveperformance and cyclic stability of MoS_2, J. Energy Storage 27 (2020), 1010782, https://doi.org/10.1016/j.est.2019.101078.

[8] R.N. Bulakhe, V.H. Nguyen, J.J. Shim, Layer-structured nanohybrid MoS_2@rGO on 3D nickel foam for high performance energy storage applications, New J. Chem. 41 (4) (2017) 1473–1482, https://doi.org/10.1039/C6NJ02590K.

[9] N. Choudhary, M.R. Islam, N. Kang, L. Tetard, Y. Jung, S.I. Khondaker, Two-dimensional lateral heterojunction through bandgap engineering of MoS_2 via oxygen plasma, J. Phys. Condens. Matter 28 (36) (2016), 364002, https://doi.org/10.1088/0953-8984/28/36/364002.

[10] M. Chandran, A. Thomas, A. Raveendran, M. Vinob, M. Bhagiyalakshmi, MoS_2 confine MXene heterostructures as electrode material for energy storage application, J. Energy Storage 30 (2020), 101446, https://doi.org/10.1016/j.est.2020.101446.

[11] M. Chen, et al., Smart combination of three-dimensional-flower-like MoS_2 nanospheres/interconnected carbon nanotubes for application in supercapacitor with enhanced electrochemical performance, J. Alloy. Compd. 696 (2017) 900–906, https://doi.org/10.1016/j.jallcom.2016.12.077.

[12] X. Geng, et al., Two-dimensional water-coupled metallic MoS_2 with nanochannels for ultrafast supercapacitors, Nano Lett. 17 (3) (2017) 1825–1832, https://doi.org/10.1021/acs.nanolett.6b05134.

[13] F. Ghasemi, M. Jalali, A. Abdollahi, S. Mohammadi, Z. Sanaee, S. Mohajerzadeh, A high performance supercapacitor based on decoration of MoS_2/reduced graphene oxide with NiO nanoparticles, RSC Adv. 7 (83) (2017) 52772–52781, https://doi.org/10.1039/c7ra09060a.

[14] W.J. Zhang, K.J. Huang, A review of recent progress in molybdenum disulfide-based supercapacitors and batteries, Inorg. Chem. Front. 4 (10) (2017) 1602–1620, https://doi.org/10.1039/c7qi00515f.

[15] T.W. Lin, T. Sadhasivam, A.Y. Wang, T.Y. Chen, J.Y. Lin, L.D. Shao, Ternary composite nanosheets with MoS_2/WS_2/graphene heterostructures as high-performance cathode materials for supercapacitors, ChemElectroChem 5 (7) (2018) 1024–1031, https://doi.org/10.1002/celc.201800043.

[16] N. Choudhary, M.R. Islam, N. Kang, L. Tetard, Y. Jung, S.I. Khondaker, Two-dimensional lateral heterojunction through bandgap engineering of MoS_2 via oxygen plasma, J. Phys. Condens. Matter 28 (36) (2016), 364002, https://doi.org/10.1088/0953-8984/28/36/364002.

[17] M.R. Islam, et al., Tuning the electrical property via defect engineering of single layer MoS_2 by oxygen plasma, Nanoscale 6 (17) (2014) 10033–10039, https://doi.org/10.1039/c4nr02142h.

[18] U. Bhanu, M.R. Islam, L. Tetard, S.I. Khondaker, Photoluminescence quenching in gold-MoS_2 hybrid nanoflakes, Sci. Rep. 4 (2014) 1–5, https://doi.org/10.1038/srep05575.

[19] S.I. Khondaker, M.R. Islam, Bandgap engineering of MoS_2 flakes via oxygen plasma: a layer dependent study, J. Phys. Chem. C 120 (25) (2016) 13801–13806, https://doi.org/10.1021/acs.jpcc.6b03247.

[20] X. Huang, Z. Zeng, H. Zhang, Metal dichalcogenide nanosheets: preparation, properties and applications, Chem. Soc. Rev. 42 (5) (2013) 1934–1946, https://doi.org/10.1039/C2CS35387C.

[21] C. Sha, et al., 3D ternary nanocomposites of molybdenum disulfide/polyaniline/reduced graphene oxide aerogel for high performance supercapacitors, Carbon 99 (2016) 26–34, https://doi.org/10.1016/j.carbon.2015.11.066. N Y.

[22] R. Wang, et al., Elucidating the intercalation pseudocapacitance mechanism of MoS$_2$-carbon monolayer interoverlapped superstructure: toward high-performance sodium-ion-based hybrid supercapacitor, ACS Appl. Mater. Interfaces 9 (38) (2017) 32745–32755, https://doi.org/10.1021/acsami.7b09813.

[23] M.B. Wazir, et al., Synergistic properties of molybdenum disulfide (MoS$_2$) with electro-active materials for high-performance supercapacitors, Int. J. Hydrog. Energy 44 (33) (2019) 17470–17492, https://doi.org/10.1016/j.ijhydene.2019.04.265.

[24] A. Borenstein, O. Hanna, R. Attias, S. Luski, T. Brousse, D. Aurbach, Carbon-based composite materials for supercapacitor electrodes: a review, J. Mater. Chem. A 5 (25) (2017) 12653–12672, https://doi.org/10.1039/c7ta00863e.

[25] Y. Shen, et al., Boosting the interface reaction activity and kinetics of cobalt molybdate by phosphating treatment for aqueous zinc-ion batteries with high energy density and long cycle life, J. Mater. Chem. A 8 (40) (2020) 21044–21052, https://doi.org/10.1039/D0TA07746A.

[26] S. Ramesh, K. Karuppasamy, A. Sivasamy, H.S. Kim, H.M. Yadav, H.S. Kim, Core shell nanostructured of Co$_3$O$_4$@RuO$_2$ assembled on nitrogen-doped graphene sheets electrode for an efficient supercapacitor application, J. Alloy. Compd. 877 (2021), 160297, https://doi.org/10.1016/j.jallcom.2021.160297.

[27] S. Ramesh, K. Karuppasamy, Y. Haldorai, A. Sivasamy, H.S. Kim, H.S. Kim, Hexagonal nanostructured cobalt oxide @ nitrogen doped multiwalled carbon nanotubes/polypyyrole composite for supercapacitor and electrochemical glucose sensor, Colloids Surf. B Biointerfaces 205 (2021), 111840, https://doi.org/10.1016/j.colsurfb.2021.111840.

[28] S. Ramesh, et al., Cubic nanostructure of Co3O4@nitrogen doped graphene oxide/polyindole composite efficient electrodes for high performance energy storage applications, J. Mater. Res. Technol. 9 (5) (2020) 11464–11475, https://doi.org/10.1016/j.jmrt.2020.08.037.

[29] C. Bathula, et al., Highly efficient solid-state synthesis of Co$_3$O$_4$ on multiwalled carbon nanotubes for supercapacitors, J. Alloy. Compd. 887 (2021), 161307, https://doi.org/10.1016/j.jallcom.2021.161307.

[30] Y. Zhao, et al., Facile synthesis of interconnected carbon network decorated with Co$_3$O$_4$ nanoparticles for potential supercapacitor applications, Appl. Surf. Sci. 487 (2019) 442–451, https://doi.org/10.1016/j.apsusc.2019.05.142.

[31] D. Liang, et al., MoS$_2$ nanosheets decorated with ultrafine Co$_3$O$_4$ nanoparticles for high-performance electrochemical capacitors, Electrochim. Acta 182 (2015) 376–382, https://doi.org/10.1016/j.electacta.2015.09.085.

[32] B. Wang, et al., Hierarchical mesoporous Co3O4/C@MoS$_2$ core–shell structured materials for electrochemical energy storage with high supercapacitive performance, Synth. Met. 233 (2017) 101–110, https://doi.org/10.1016/j.synthmet.2017.09.011.

[33] J. Wang, H. Zhou, M. Zhu, A. Yuan, X. Shen, Metal-organic framework-derived Co$_3$O$_4$ covered by MoS$_2$ nanosheets for high-performance lithium-ion batteries, J. Alloy. Compd. 744 (2018) 220–227, https://doi.org/10.1016/j.jallcom.2018.02.086.

[34] Y. Lou, et al., Nanocomposite of ultrasmall Co$_3$O$_4$ nanoparticles deposited on ultrathin MoS$_2$ surfaces for excellent performance anode materials in lithium ion batteries, Chem. Eng. J. 313 (2017) 1269–1277, https://doi.org/10.1016/j.cej.2016.11.015.

[35] Y. Zhang, T. He, G. Liu, L. Zu, J. Yang, One-pot mass preparation of MoS$_2$/C aerogels for high-performance supercapacitors and lithium-ion batteries, Nanoscale 9 (28) (2017) 10059–10066, https://doi.org/10.1039/c7nr03187d.

[36] N. Feng, et al., A polymer-direct-intercalation strategy for MoS$_2$/carbon-derived heteroaerogels with ultrahigh pseudocapacitance, Nat. Commun. 10 (1) (2019), https://doi.org/10.1038/s41467-019-09384-7.

[37] T. Stephenson, Z. Li, B. Olsen, D. Mitlin, Lithium ion battery applications of molybdenum disulfide (MoS$_2$) nanocomposites, Energy Environ. Sci. 7 (1) (2014) 209–231, https://doi.org/10.1039/c3ee42591f.

[38] E. Pomerantseva, Y. Gogotsi, Two-dimensional heterostructures for energy storage, Nat. Energy 2 (7) (2017) 1–6, https://doi.org/10.1038/nenergy.2017.89.

[39] X. Zhang, Z. Lai, C. Tan, H. Zhang, Solution-processed two-dimensional MoS$_2$ nanosheets: preparation, hybridization, and applications, Angew. Chem. Int. Ed. 55 (31) (2016) 8816–8838, https://doi.org/10.1002/anie.201509933.

[40] X. Wang, et al., High supercapacitor and adsorption behaviors of flower-like MoS$_2$ nanostructures, J. Mater. Chem. A 2 (38) (2014) 15958–15963, https://doi.org/10.1039/C4TA03044C.

[41] Z. Wu, B. Li, Y. Xue, J. Li, Y. Zhang, F. Gao, Fabrication of defect-rich MoS$_2$ ultrathin nanosheets for application in lithium-ion batteries and supercapacitors, J. Mater. Chem. A 3 (38) (2015) 19445–19454, https://doi.org/10.1039/C5TA04549E.

[42] B.H. Park, J.H. Choi, Improvement in the capacitance of a carbon electrode prepared using water-soluble polymer binder for a capacitive deionization application, Electrochim. Acta 55 (8) (2010) 2888–2893, https://doi.org/10.1016/j.electacta.2009.12.084.

[43] H.K. Park, B.S. Kong, E.S. Oh, Effect of high adhesive polyvinyl alcohol binder on the anodes of lithium ion batteries, Electrochem. Commun. 13 (10) (2011) 1051–1053, https://doi.org/10.1016/j.elecom.2011.06.034.

[44] N. Thi Xuyen, J.M. Ting, Hybridized 1T/2H MoS$_2$ having controlled 1T concentrations and its use in supercapacitors, Chem. Eur. J. 23 (68) (2017) 17348–17355, https://doi.org/10.1002/chem.201703690.

[45] H. Fu, et al., Enhanced field emission and photocatalytic performance of MoS$_2$ titania nanoheterojunctions via two synthetic approaches, Dalton Trans. 44 (4) (2015) 1664–1672, https://doi.org/10.1039/c4dt03035d.

[46] F. Xiong, et al., Three-dimensional crumpled reduced graphene oxide/MoS$_2$ nanoflowers: a stable anode for lithium-ion batteries, ACS Appl. Mater. Interfaces 7 (23) (2015) 12625–12630, https://doi.org/10.1021/acsami.5b02978.

[47] Y.B. Li, Y. Bando, D. Golberg, MoS$_2$ nanoflowers and their field-emission properties, Appl. Phys. Lett. 82 (12) (2003) 1962–1964, https://doi.org/10.1063/1.1563307.

[48] B. Liu, X. Zhang, H. Shioyama, T. Mukai, T. Sakai, Q. Xu, Converting cobalt oxide subunits in cobalt metal-organic framework into agglomerated Co$_3$O$_4$ nanoparticles as an electrode material for lithium ion battery, J. Power Sources 195 (3) (2010) 857–861, https://doi.org/10.1016/j.jpowsour.2009.08.058.

[49] B.B. Li, et al., Pd coated MoS$_2$ nanoflowers for highly efficient hydrogen evolution reaction under irradiation, J. Power Sources 284 (2015) 68–76, https://doi.org/10.1016/j.jpowsour.2015.03.021.

[50] D. Wang, Z. Pan, Z. Wu, Z. Wang, Z. Liu, Hydrothermal synthesis of MoS$_2$ nanoflowers as highly efficient hydrogen evolution reaction catalysts, J. Power Sources 264 (2014) 229–234, https://doi.org/10.1016/j.jpowsour.2014.04.066.

[51] Y. Feldman, E. Wasserman, D.J. Srolovitz, R. Tenne, High-rate, gas-phase growth of MoS$_2$ nested inorganic fullerenes and nanotubes, Science 267 (5195) (1995) 222–225, https://doi.org/10.1126/science.267.5195.222.

[52] Y. Zhang, et al., Defect-like structures of graphene on copper foils for strain relief investigated by high-resolution scanning tunneling microscopy, ACS Nano 5 (5) (2011) 4014–4022, https://doi.org/10.1021/nn200573v.

[53] Z. Wu, et al., Enhanced hydrogen evolution catalysis from osmotically swollen ammoniated MoS$_2$, J. Mater. Chem. A 3 (24) (2015) 13050–13056, https://doi.org/10.1039/C5TA02010G.

[54] K.D. Rasamani, F. Alimohammadi, Y. Sun, Interlayer-expanded MoS$_2$, Mater. Today 20 (2) (2017) 83–91, https://doi.org/10.1016/j.mattod.2016.10.004.

[55] L. Hu, Y. Ren, H. Yang, Q. Xu, Fabrication of 3D hierarchical MoS$_2$/polyaniline and MoS$_2$/C architectures for lithium-ion battery applications, ACS Appl. Mater. Interfaces 6 (16) (2014) 14644–14652, https://doi.org/10.1021/am503995s.

[56] X. Ding, Y. Huang, S. Li, N. Zhang, J. Wang, 3D architecture reduced graphene oxide-MoS$_2$ composite: preparation and excellent electromagnetic wave absorption performance, Compos. Part A 90 (2016) 424–432, https://doi.org/10.1016/j.compositesa.2016.08.006.

[57] M. Chen, et al., Smart combination of three-dimensional-flower-like MoS$_2$ nanospheres/interconnected carbon nanotubes for application in supercapacitor with enhanced electrochemical performance, J. Alloy. Compd. 696 (2017) 900–906, https://doi.org/10.1016/j.jallcom.2016.12.077.

[58] S. Dutta, S. De, MoS$_2$ nanosheet/rGO hybrid: an electrode material for high performance thin film supercapacitor, Mater. Today Proc. 5 (3) (2018) 9771–9775, https://doi.org/10.1016/j.matpr.2017.10.165.

[59] H. Song, A. Tang, G. Xu, L. Liu, Y. Pan, M. Yin, Hydrothermal synthesis and electrochemical properties of MoS$_2$/C nanocomposite, Int. J. Electrochem. Sci. 13 (7) (2018) 6708–6716, https://doi.org/10.20964/2018.07.54.

[60] H. Li, K. Yu, X. Lei, B. Guo, H. Fu, Z. Zhu, Hydrothermal synthesis of novel MoS$_2$/BiVO$_4$ hetero-nanoflowers with enhanced photocatalytic activity and a mechanism investigation, J. Phys. Chem. C 119 (39) (2015) 22681–22689, https://doi.org/10.1021/acs.jpcc.5b06729.

[61] L. Ma, L. Xu, X. Xu, X. Zhou, J. Luo, L. Zhang, Cobalt-doped edge-rich MoS$_2$/nitrogenated graphene composite as an electrocatalyst for hydrogen evolution reaction, Mater. Sci. Eng. B Solid State Mater. Adv. Technol. 212 (2016) 30–38, https://doi.org/10.1016/j.mseb.2016.07.014.

[62] D. Wang, X. Zhang, Y. Shen, Z. Wu, Ni-doped MoS$_2$ nanoparticles as highly active hydrogen evolution electrocatalysts, RSC Adv. 6 (20) (2016) 16656–16661, https://doi.org/10.1039/c6ra02610a.

[63] X.J. Lv, G.W. She, S.X. Zhou, Y.M. Li, Highly efficient electrocatalytic hydrogen production by nickel promoted molybdenum sulfide microspheres catalysts, RSC Adv. 3 (44) (2013) 21231–21236, https://doi.org/10.1039/c3ra42340a.

[64] V. Radmilović, H.A. Gasteiger, P.N. Ross, Structure and chemical composition of a supported Pt-Ru electrocatalyst for methanol oxidation, J. Catal. 154 (1) (1995) 98–106, https://doi.org/10.1006/jcat.1995.1151.

[65] W.S. Hummers, R.E. Offeman, Preparation of graphitic oxide, J. Am. Chem. Soc. 80 (6) (1958) 1339, https://doi.org/10.1021/ja01539a017.

[66] K.K. Paul, N. Sreekanth, R.K. Biroju, T.N. Narayanan, P.K. Giri, Solar light driven photoelectrocatalytic hydrogen evolution and dye degradation by metal-free few-layer MoS$_2$ nanoflower/TiO$_2$(B) nanobelts heterostructure, Sol. Energy Mater. Sol. Cells 185 (2018) 364–374, https://doi.org/10.1016/j.solmat.2018.05.056. October 2017.

[67] G. Du, Z. Guo, S. Wang, R. Zeng, Z. Chen, H. Liu, Superior stability and high capacity of restacked molybdenum disulfide as anode material for lithium ion batteries, Chem. Commun. 46 (7) (2010) 1106–1108, https://doi.org/10.1039/b920277c.

[68] X. Zhang, et al., Facile synthesis of yolk–shell MoO$_2$ microspheres with excellent electrochemical performance as a Li-ion battery anode, J. Mater. Chem. A 1 (23) (2013) 6858–6864, https://doi.org/10.1039/C3TA10399D.

[69] X. Zhang, et al., Hydrothermal synthesis and characterization of 3D flower-like MoS$_2$ microspheres, Mater. Lett. 148 (2015) 67–70, https://doi.org/10.1016/j.matlet.2015.02.027.

[70] X. Wang, Z. Zhang, Y. Chen, Y. Qu, Y. Lai, J. Li, Morphology-controlled synthesis of MoS$_2$ nanostructures with different lithium storage properties, J. Alloy. Compd. 600 (2014) 84–90, https://doi.org/10.1016/j.jallcom.2014.02.127.

[71] A.A. Akl, A.S. Hassanien, Microstructure and crystal imperfections of nanosized CdSxSe1-x thermally evaporated thin films, Superlattices Microstruct. 85 (2015) 67–81, https://doi.org/10.1016/j.spmi.2015.05.011.

[72] Q. Fan, A new method of calculating interplanar spacing: the position-factor method, J. Appl. Crystallogr. 45 (6) (2012) 1303–1308, https://doi.org/10.1107/S0021889812037764.

[73] G. Tang, Y. Wang, W. Chen, H. Tang, C. Li, Hydrothermal synthesis and characterization of novel flowerlike MoS$_2$ hollow microspheres, Mater. Lett. 100 (2013) 15–18, https://doi.org/10.1016/j.matlet.2013.02.103.

[74] R. Zhou, C. jie Han, X. min Wang, Hierarchical MoS$_2$-coated three-dimensional graphene network for enhanced supercapacitor performances, J. Power Sources 352 (2017) 99–110, https://doi.org/10.1016/j.jpowsour.2017.03.134.

[75] X. Li, L. Zhang, X. Zang, X. Li, H. Zhu, Photo-promoted platinum nanoparticles decorated MoS$_2$@graphene woven fabric catalyst for efficient hydrogen generation, ACS Appl. Mater. Interfaces 8 (17) (2016) 10866–10873, https://doi.org/10.1021/acsami.6b01903.

[76] A. Gigot, et al., Mixed 1T-2H phase MoS$_2$/reduced graphene oxide as active electrode for enhanced supercapacitive performance, ACS Appl. Mater. Interfaces 8 (48) (2016) 32842–32852, https://doi.org/10.1021/acsami.6b11290.

[77] P.A. Bertrand, Surface-phonon dispersion of MoS$_2$, Phys. Rev. B 44 (11) (1991) 5745–5749, https://doi.org/10.1103/PhysRevB.44.5745.

[78] P.A. Bertrand, Surface-phonon dispersion of MoS$_2$, Phys. Rev. B 44 (11) (1991) 5745–5749.

[79] K.K. Liu, et al., Growth of large-area and highly crystalline MoS$_2$ thin layers on insulating substrates, Nano Lett. 12 (3) (2012) 1538–1544, https://doi.org/10.1021/nl2043612.

[80] D. Wang, Z. Pan, Z. Wu, Z. Wang, Z. Liu, Hydrothermal synthesis of MoS$_2$ nanoflowers as highly efficient hydrogen evolution reaction catalysts, J. Power Sources 264 (2014) 229–234, https://doi.org/10.1016/j.jpowsour.2014.04.066.

[81] Z. Wang, et al., CTAB-assisted synthesis of single-layer MoS$_2$–graphene composites as anode materials of Li-ion batteries, J. Mater. Chem. A 1 (6) (2013) 2202–2210, https://doi.org/10.1039/C2TA00598K.

[82] H. Li, et al., From bulk to monolayer MoS$_2$: evolution of Raman scattering, Adv. Funct. Mater. 22 (7) (2012) 1385–1390, https://doi.org/10.1002/adfm.201102111.

[83] B. Chakraborty, A. Bera, D.V.S. Muthu, S. Bhowmick, U.V. Waghmare, A.K. Sood, Symmetry-dependent phonon renormalization in monolayer MoS$_2$ transistor, Phys. Rev. B Condens. Matter Mater. Phys. 85 (16) (2012) 2–5, https://doi.org/10.1103/PhysRevB.85.161403.

[84] Y. Shi, et al., Selective decoration of Au nanoparticles on monolayer MoS$_2$ single crystals, Sci. Rep. 3 (2013) 1–7, https://doi.org/10.1038/srep01839.

[85] H. Li, et al., From bulk to monolayer MoS$_2$: evolution of Raman scattering, Adv. Funct. Mater. 22 (7) (2012) 1385–1390, https://doi.org/10.1002/adfm.201102111.

[86] Y. Gogotsi, R.M. Penner, Energy storage in nanomaterials − capacitive, pseudocapacitive, or battery-like? ACS Nano 3 (12) (2018) 2081–2083, https://doi.org/10.1021/acsnano.8b01914.

[88] Y. Chen, W. Ma, K. Cai, X. Yang, C. Huang, Electrochimica acta *in situ* growth of polypyrrole onto three-dimensional tubular MoS$_2$ as an advanced negative electrode material for supercapacitor, Electrochim. Acta 246 (2017) 615–624, https://doi.org/10.1016/j.electacta.2017.06.102.

[87] F. Yang, et al., *In situ* construction of heterostructured bimetallic sulfide/phosphide with rich interfaces for high-performance aqueous Zn-ion batteries, Sci. China Mater. (2021), https://doi.org/10.1007/s40843-021-1739-0.

[89] A.K. Thakur, A.B. Deshmukh, R. Bilash, I. Karbhal, M. Majumder, M.V. Shelke, Facile synthesis and electrochemical evaluation of PANI/CNT/MoS$_2$ ternary composite as an electrode material for high performance supercapacitor, Materials Science & Engineering B 223 (2017) 24–34, https://doi.org/10.1016/j.mseb.2017.05.001.

[90] R.N. Vyas, K. Li, B. Wang, Modifying randles circuit for analysis of polyoxometalate layer-by-layer films, J. Phys. Chem. B 114 (48) (2010) 15818–15824, https://doi.org/10.1021/jp105075t.

[91] M.R. Islam, S.M.N.S. Pias, R.B. Alam, S.I. Khondaker, Enhanced electrochemical performance of solution-processed single-wall carbon nanotube reinforced polyvinyl alcohol nanocomposite synthesized via solution-cast method, Nano Express 1 (3) (2020), 030013, https://doi.org/10.1088/2632-959x/abc050.

[92] H.M. Yadav, et al., Nickel-graphene nanoplatelet deposited on carbon fiber as binder-free electrode for electrochemical supercapacitor application, Polymers 12 (8) (2020), https://doi.org/10.3390/polym12081666 (Basel).

[93] P.K. Basivi, et al., Ultrasonication-mediated nitrogen-doped multiwalled carbon nanotubes involving carboxy methylcellulose composite for solid-state supercapacitor applications, Sci. Rep. 11 (1) (2021) 9918, https://doi.org/10.1038/s41598-021-89430-x.

[94] M.R. Islam, S.I. Mollik, Enhanced electrochemical performance of flexible and eco-friendly starch/graphene oxide nanocomposite, Heliyon 6 (10) (2020), https://doi.org/10.1016/j.heliyon.2020.e05292.

[95] D. Li, et al., Transparent 1T-MoS2 nanofilm robustly anchored on substrate by layer-by-layer self-assembly and its ultra-high cycling stability as supercapacitors, Nanotechnology 28 (39) (2017), 395401, https://doi.org/10.1088/1361-6528/aa7ee3.

[96] C. Nagaraju, C.V.V.M. Gopi, J.W. Ahn, H.J. Kim, Hydrothermal synthesis of MoS$_2$ and WS$_2$ nanoparticles for high-performance supercapacitor applications, New J. Chem. 42 (15) (2018) 12357–12360, https://doi.org/10.1039/c8nj02822b.

[97] W. Wang, et al., Hydrous ruthenium oxide nanoparticles anchored to graphene and carbon nanotube hybrid foam for supercapacitors, Sci. Rep. 4 (ii) (2014) 9–14, https://doi.org/10.1038/srep04452, no.

[98] S.S. Singha, et al., Mn incorporated MoS2 nanoflowers: a high performance electrode material for symmetric supercapacitor, Electrochim. Acta 338 (2020), https://doi.org/10.1016/j.electacta.2020.135815.

[99] S. Wang, et al., Three-dimensional MoS$_2$@CNT/RGO network composites for high-performance flexible supercapacitors, Chem. Eur. J. 23 (14) (2017) 3438–3446, https://doi.org/10.1002/chem.201605465.

[100] J. Wang, J. Polleux, J. Lim, B. Dunn, Pseudocapacitive contributions to electrochemical energy storage in TiO$_2$ (anatase) nanoparticles, J. Phys. Chem. C 111 (40) (2007) 14925–14931, https://doi.org/10.1021/jp074464w.

[101] E. Rafiee, M. Farzam, M.A. Golozar, A. Ashrafi, An Investigation on dislocation density in cold-rolled copper using electrochemical impedance spectroscopy, ISRN Corros. 2013 (2013) 1–6, https://doi.org/10.1155/2013/921825, vol.

[102] N. Savjani, et al., Synthesis of lateral size-controlled monolayer 1H-MoS$_2$@ oleylamine as supercapacitor electrodes, Chem. Mater. 28 (2) (2016) 657–664, https://doi.org/10.1021/acs.chemmater.5b04476.

[103] D. Li, et al., Design and electrosynthesis of monolayered MoS$_2$ and BF4−-doped poly(3,4-ethylenedioxythiophene) nanocomposites for enhanced supercapacitive performance, J. Electroanal. Chem. 801 (2017) 345–353, https://doi.org/10.1016/j.jelechem.2017.08.012, no. August.

[104] L. Wang, X. Zhang, Y. Ma, M. Yang, Y. Qi, Supercapacitor performances of the MoS$_2$/CoS$_2$ nanotube arrays *in situ* grown on ti plate, J. Phys. Chem. C 121 (17) (2017) 9089–9095, https://doi.org/10.1021/acs.jpcc.6b13026.

[105] M.A. Bissett, I.A. Kinloch, R.A.W. Dryfe, Characterization of MoS$_2$-graphene composites for high-performance coin cell supercapacitors, ACS Appl. Mater. Interfaces 7 (31) (2015) 17388–17398, https://doi.org/10.1021/acsami.5b04672.

[106] Y. Chen, X. Zhu, D. Yang, P. Wangyang, B. Zeng, H. Sun, A novel design of poly (3,4-ethylenedioxythiophene):poly (styrenesulfonate)/molybdenum disulfide/poly (3,4-ethylenedioxythiophene) nanocomposites for fabric micro-supercapacitors with favourable performances, Electrochim. Acta 298 (2019) (2019) 297–304, https://doi.org/10.1016/j.electacta.2018.12.083, no.

[107] K. Zhang, X. Ye, Y. Shen, Z. Cen, K. Xu, F. Yang, Interface engineering of Co$_3$O$_4$ nanowire arrays with ultrafine NiO nanowires for high-performance rechargeable alkaline batteries, Dalton Trans. 49 (25) (2020) 8582–8590, https://doi.org/10.1039/D0DT01556C.